FERMILAB-PUB-08-210

The MiniBooNE Detector

The MiniBooNE Collaboration

A. A. Aguilar-Arevalo[e], C. E. Anderson[p], L. M. Bartoszek[g], A. O. Bazarko[m], S. J. Brice[g], B. C. Brown[g], L. Bugel[e], J. Cao[ℓ], L. Coney[e], J. M. Conrad[e], D. C. Cox[i], A. Curioni[p], Z. Djurcic[e], D. A. Finley[g], B. T. Fleming[p], R. Ford[g], F. G. Garcia[g], G. T. Garvey[j], C. Green[j,g], J. A. Green[i,j], T. L. Hart[d], E. Hawker[j,c], R. Imlay[k], R. A. Johnson[c], G. Karagiorgi[e], P. Kasper[g], T. Katori[i], T. Kobilarcik[g], I. Kourbanis[g], S. Koutsoliotas[b], E. M. Laird[m], S. K. Linden[p], J. M. Link[o], Y. Liu[ℓ], Y. Liu[a], W. C. Louis[j], K. B. M. Mahn[e], W. Marsh[g], P. S. Martin[g], G. McGregor[j], W. Metcalf[k], H.-O. Meyer[i], P. D. Meyers[m], F. Mills[g], G. B. Mills[j], J. Monroe[e], C. D. Moore[g], R. H. Nelson[d], V. T. Nguyen[e], P. Nienaber[n], J. A. Nowak[k], S. Ouedraogo[k], R. B. Patterson[m], D. Perevalov[a], C. C. Polly[i], E. Prebys[g], J. L. Raaf[c], H. Ray[j,h], B. P. Roe[ℓ], A. D. Russell[g], V. Sandberg[j], W. Sands[m], R. Schirato[j], G. Schofield[k], D. Schmitz[e], M. H. Shaevitz[e], F. C. Shoemaker[m], D. Smith[f], M. Soderberg[p], M. Sorel[e][1], P. Spentzouris[g], I. Stancu[a], R. J. Stefanski[g], M. Sung[k], H. A. Tanaka[m], R. Tayloe[i], M. Tzanov[d], R. Van de Water[j], M. O. Wascko[k][2], D. H. White[j], M. J. Wilking[d], H. J. Yang[ℓ], G. P. Zeller[e,j], E. D. Zimmerman[d]

[a] *University of Alabama, Tuscaloosa, AL 35487*
[b] *Bucknell University, Lewisburg, PA 17837*
[c] *University of Cincinnati, Cincinnati, OH 45221*
[d] *University of Colorado, Boulder, CO 80309*
[e] *Columbia University, New York, NY 10027*
[f] *Embry-Riddle Aeronautical University, Prescott, AZ 86301*
[g] *Fermi National Accelerator Laboratory, Batavia, IL 60510*
[h] *University of Florida, Gainesville, FL 32611*
[i] *Indiana University, Bloomington, IN 47405*

Preprint submitted to Elsevier *25 June 2008*

[j] *Los Alamos National Laboratory, Los Alamos, NM 87545*
[k] *Louisiana State University, Baton Rouge, LA 70803*
[ℓ] *University of Michigan, Ann Arbor, MI 48109*
[m] *Princeton University, Princeton, NJ 08544*
[n] *Saint Mary's University of Minnesota, Winona, MN 55987*
[o] *Virginia Polytechnic Institute & State University, Blacksburg, VA 24061*
[p] *Yale University, New Haven, CT 06520*

Abstract

The MiniBooNE neutrino detector was designed and built to look for $\nu_\mu \to \nu_e$ oscillations in the $(\sin^2 2\theta, \Delta m^2)$ parameter space region where the LSND experiment reported a signal. The MiniBooNE experiment used a beam energy and baseline that were an order of magnitude larger than those of LSND so that the backgrounds and systematic errors would be completely different. This paper provides a detailed description of the design, function, and performance of the MiniBooNE detector.

1 Introduction

1.1 Physics Overview

The MiniBooNE experiment at Fermilab was proposed to test the evidence for neutrino oscillations from the LSND experiment at Los Alamos [1]. The LSND experiment observed more $\bar{\nu}_e$ candidate events than expected from background. If the excess is interpreted as being due to $\bar{\nu}_\mu \to \bar{\nu}_e$ oscillations, then the most favored oscillation region is a band in Δm^2 stretching from $\sim$0.2 eV^2 to $\sim$2 eV^2. The MiniBooNE experiment was designed to search for $\nu_\mu \to \nu_e$ and $\bar{\nu}_\mu \to \bar{\nu}_e$ oscillations with approximately the same $L/E \simeq 1$ value as LSND, where L is the neutrino travel distance from the source to the detector in meters and E is the neutrino energy in MeV. Whereas the LSND neutrino beam travelled a distance of 30 m with a typical energy of 30 MeV, the MiniBooNE neutrino beam traveled 500 m and had a typical energy of 500 MeV. With neutrino energies an order of magnitude higher, the MiniBooNE backgrounds and systematic errors are completely different from those of LSND. MiniBooNE, therefore, constitutes an independent check of the LSND evidence for neutrino oscillations at the $\sim$1 eV^2 mass scale.

---

[1] Present address: IFIC, Universidad de Valencia and CSIC, Valencia 46071, Spain
[2] Present address: Imperial College London, London, SW7 2AZ, UK

1.2 Physics Driven Parameters

In order to search effectively for $\nu_\mu \rightarrow \nu_e$ and $\bar{\nu}_\mu \rightarrow \bar{\nu}_e$ oscillations, the MiniBooNE detector needed to satisfy certain requirements. First, the detector required a target mass of ~1 kton in order to generate ~1000 neutrino oscillation events for 10^{21} protons on target. Second, the detector needed to provide excellent discrimination between ν_μ and ν_e induced events. The scale is set by the LSND neutrino oscillation probability of ~0.26%. (The intrinsic ν_e background in MiniBooNE is ~0.5%.) Third, the detector had to have a completely active volume with no dead regions. This was necessary in order to contain neutral-current $\pi^0 \rightarrow \gamma\gamma$ events, which would constitute a large background if one of the γ's escaped detection. Fourth, the detector needed to have a 4π veto to reject cosmic ray events, neutrino interactions that occur outside the detector, and neutrino events with tracks that escape the fiducial volume. Liquid Cherenkov detectors have no dead regions, have an easily configured veto region, and, thanks to modern computers, have excellent particle identification. A liquid Cherenkov detector is an economical choice that meets all of these requirements.

1.3 Overall Design Considerations and Constraints

Mineral oil was chosen instead of water as the liquid for the MiniBooNE detector for several reasons. First, mineral oil has an index of refraction $n = 1.47$, which is considerably higher than the $n = 1.33$ index of refraction for water. This higher index of refraction, together with a lower density than water (0.85 $\mathrm{gm/cm^3}$ instead of 1.00 $\mathrm{gm/cm^3}$), means that electrons produce considerably more Cherenkov light in mineral oil than in water. Furthermore, the lower velocity of light in mineral oil improves the event position reconstruction. Second, mineral oil allows the detection of lower-energy muons, pions, and protons than in water due to the lower Cherenkov threshold and the presence of scintillation light in pure mineral oil. This is used for background rejection and for measuring backgrounds down to lower energies. Third, mineral oil has less multiple scattering than water and a smaller μ^- capture rate, 8% compared to 20% in water. The smaller μ^- capture rate increases the efficiency of the identification of charged-current reactions using the Michel electron tag from muon decay. Mineral oil has the additional advantage that one can safely immerse electronic components in it. The downside of mineral oil is that it requires a much more complicated optical model to describe the generation and transmission of light through the medium (see Sec. 3.2).

As the photomultiplier tube (PMT) coverage for a liquid Cherenkov detector is proportional to the detector surface area, a spherical tank was chosen to

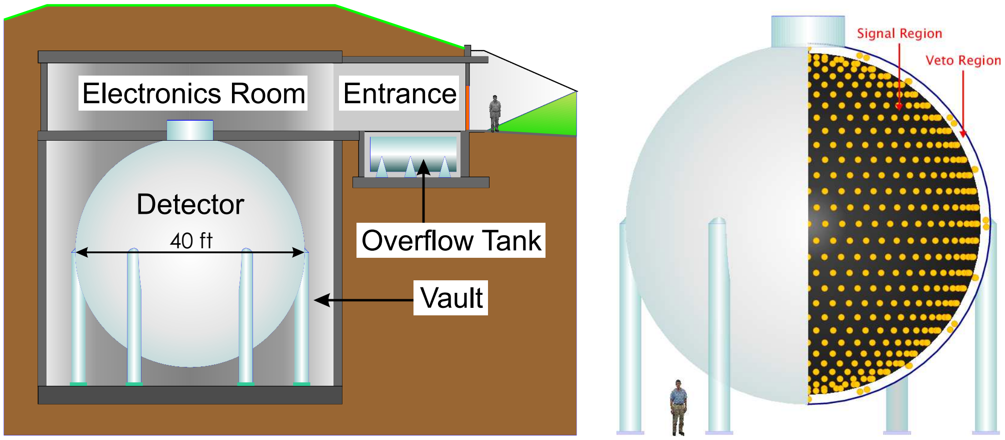

Fig. 1. The MiniBooNE detector enclosure (left) and a cut-away drawing (right) of the detector showing the distribution of PMT's in the signal and veto regions.

maximize the ratio of volume to surface area. Furthermore, a spherical geometry has no inside edges which is beneficial for the event reconstruction. The detector (see Fig. 1) is a spherical tank of diameter 12.2 m (40 ft), which is filled with 818 tons of mineral oil. An opaque barrier divides the volume into an inside main detector region and an outside veto region and supports the PMT's viewing the main detector region.

In order to reduce the detector cost, the collaboration chose to reuse the LSND phototubes (∼1220) and electronics (∼1600 channels). An additional 330 phototubes were purchased in order to obtain a total phototube channel count of 1520 after rejection of the poorest tubes. The allocation of PMT's in the main tank and veto and the thickness of the veto region were determined by physics considerations and were arrived at using Monte Carlo simulations of signal and background events. The Monte Carlo studies used a full GEANT simulation, including tracking of individual Cherenkov and scintillation photons, with wavelength-dependent absorption, reflection, and detection efficiencies. Analysis of events in the main tank indicated that at least 10% photocathode coverage (defined by treating the photocathodes as flat disks with diameter equal to the PMT diameter) was needed to provide the required particle identification quality. When tuned to the secondary requirement that veto and main tank channels not be mixed in the same electronics crate, a final number of 1280 tank PMT's resulted. Calculated with the final radial position, this allocation has a photocathode coverage of 11.3%.

This allowed 240 veto PMT's, and the issue was whether the veto region would yield sufficient light to reject muons from cosmic rays and beam-neutrino interactions outside the tank with an efficiency >99%, the design goal. Monte Carlo studies, including estimates of the albedo of the painted surfaces in the veto (see Sec. 4.2), indicated that the light yield with a 35 cm veto thickness was high enough to allow reasonable thresholds in the face of noise and an estimate of light leaked from the main tank. Separate calculations showed that loss of signal due to muon tracks hiding in the struts and cables that penetrate the veto region was negligible. The actual efficiency for rejecting cosmic ray muons was measured to be 99.99% (see Sec. 8.3). The 35 cm veto thickness puts the optical barrier at a radius of 574.6 cm.

1.4 Experiment Layout

Protons with 8 GeV kinetic energy are extracted from the Fermilab Booster and transported to the MiniBooNE target hall which contains a beryllium target within a magnetic focusing horn. The target and horn are followed by a pion decay volume at the end of which is a 3.8 m thick steel and concrete beam dump. The distance from the center of the target to the front face of the dump is 50 m.

The neutrino beam [2] that is produced in the decay volume passes through the dump plus 474 m of earth before reaching the MiniBooNE detector vault. This ensures that neutrinos are the only beam products that can reach the detector. The total distance from the upstream face of the target to the center of the detector is 541 m.

The detector tank, as shown in Fig. 1, sits below ground level inside a 13.7 m (45 ft) diameter cylindrical vault with a room above that houses electronics and utilities. The vault not only provides access to the tank's exterior plumbing, but also acts as secondary containment for the mineral oil. The entire structure is covered by at least 3 m of dirt which provides shielding against cosmic ray backgrounds and makes it easier to keep the detector at a constant temperature.

2 Photomultiplier Tubes

2.1 PMT Specification

The PMT's used in MiniBooNE were 8 inch Hamamatsu tubes of two types: 1198 were R1408's recycled from LSND, and 322 were newer R5912 tubes. As detailed in Ref. [3], all the PMT's were tested before installation to determine their relevant properties: gain, dark noise rate, charge resolution, timing resolution, and double pulsing rate. As the new tubes have better time and charge resolution, all were used in the main tank, distributed randomly. The older tubes with the lowest dark noise rate were used in the veto and the rest completed the main tank array. The array of tubes deployed in the main tank

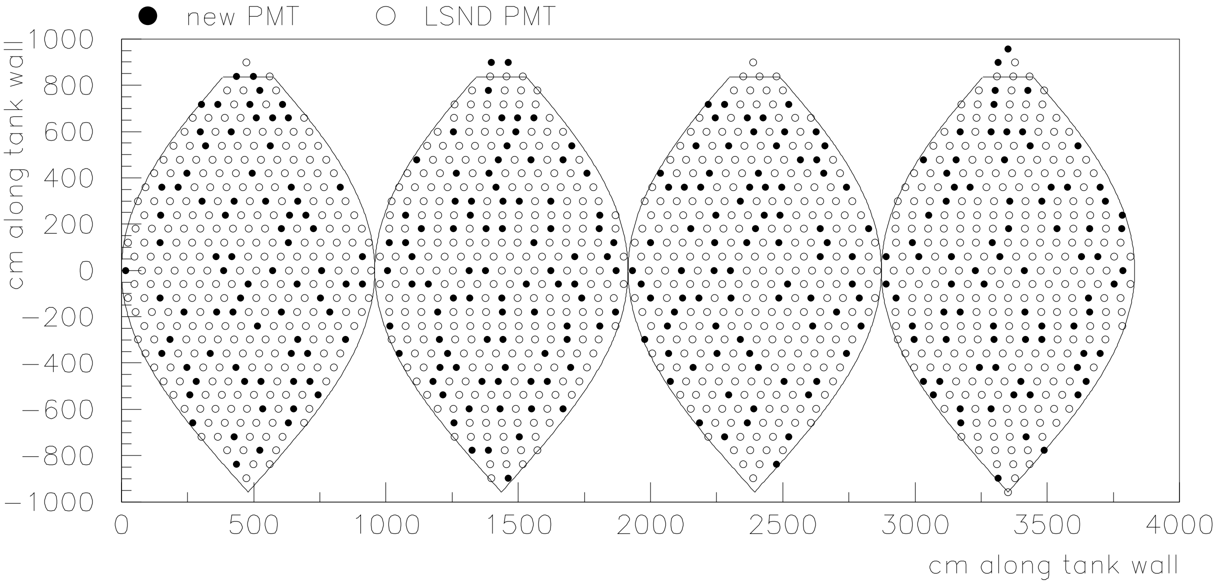

Fig. 2. Main phototube layout. PMT's are not drawn to scale.

is shown in Fig. 2.

These PMT's have a wavelength dependent efficiency that, as shown in Fig. 13, peaks at 390 nm, falling to half its maximum at 315 and 490 nm [4]. The MiniBooNE PMT's are operated with ∼2000 V (positive) on the dynode chain, resulting in a gain of $\sim 1.6 \times 10^7$. The intrinsic time resolution of the PMT's is ∼1 ns, and the intrinsic charge resolution is ∼15% at 1 p.e [5]. Although the time and charge measurements are smeared by the data acquisition electronics, the dominant contribution to the resolutions results from the intrinsic PMT properties.

2.2 PMT preparation

After the PMT's had their bases attached, were tested, and were assigned to a location in the tank, they were prepared for installation.

- Each tube was washed in a mild solution of detergent and distilled water, rinsed in clean distilled water, and then allowed to dry for 24 hours. The main purpose was to remove the scintillator-doped oil residue from LSND.
- New tubes were mounted in stands (see Sec. 4.1). Old tubes destined for the main tank were re-mounted in stands.
- The tube was dipped in black Master Bond EP21LV encapsulant from the base up to the bottom of the globe. This is to protect the oil from the components of the base and vice versa. Old tubes were already coated in black Hysol. This was found to contaminate mineral oil (Sec. 3.3), so the

old tubes were also dipped in Master Bond.
- Veto tubes were removed from their stands and mounted in veto mounts.
- Main tubes had the centering clips attached around the tube neck. When LSND was opened to harvest the phototubes, it was found that about 100 tubes had floated out of their stands. Consequently, a stripe of Master Bond was run down the neck of the tube over the silicone rubber cushion on each centering clip. This attachment served as a mechanical backup in case the metal band and foam tape at the tube's equator slipped.

This work was done in a cleanroom. It was found that maintaining low humidity was necessary for the proper curing of the Master Bond.

3 Mineral Oil

3.1 Oil Selection and Delivery

The MiniBooNE detector tank holds 9.5×10^5 liters of mineral oil. Because of the large path length that an optical photon must traverse in the oil, a large extinction length (attenuation of a beam due to all causes including scattering) was the most important criterion for the mineral oil chosen for MiniBooNE. An extinction length of greater than 20 m for 420 nm light was required in order to lose no more than 25 percent of the light generated by a neutrino interaction occurring in the center of the detector. Light transmission throughout the wavelength range of 320 nm to 600 nm was also considered in selecting the oil. The oil was also required to have a large index of refraction, a small dispersion over the wavelength range 320 nm to 600 nm, low reactivity with materials in the detector, low levels of scintillation light, and low viscosity [6].

Ten different oils from six different vendors were tested. Based on the above criteria, Marcol 7 Light Mineral Oil (Industrial NF grade), an Exxon/Mobil product manufactured by Penreco was selected for MiniBooNE. It was certified by the manufacturer to have a specific gravity between 0.76 and 0.87 gm/cm^3 as measured via the American Society for Testing and Materials (ASTM) D 4052 or ASTM D 1298, a viscosity less than 34.5 cSt at 40 °C as measured via ASTM D 445, and a color greater than or equal to 30 Saybolt Color units as measured via ASTM D 156. While a more dense oil would have provided more interactions in the detector, the need for recirculation imposed an upper limit on its viscosity and an implicit maximum density.

The Marcol 7 mineral oil was delivered to the Fermilab railhead in food-grade railcar tankers that were cleaned and dried before filling. Prior to shipping, the manufacturer was required to draw a sample from the bottom of each

Density	0.845 ± 0.001 g/cm^3
Coefficient of volume expansion	$(61 \pm 4) \times 10^{-5}$ K^{-1}
Refractive index, n_D(589.3 nm)	$(1.4684 \pm 0.0002)\times$ $[1 - (3.66 \pm 0.04) \times 10^{-4}(T - 20\ ^\circ\mathrm{C})]$
Dispersion (n_F(486.1 nm)-n_C(656.3 nm))	0.0081 ± 0.0003
Extinction length (at 460 nm)	25-40 m (see text)
Rayleigh scattering length (at 442 nm)	51.7 ± 7.0 m

Table 1
Some measured properties of the MiniBooNE Marcol 7 mineral oil [7].

railcar and perform the following tests using the methods shown in parentheses: specific gravity (ASTM D 4052 or D 1298), color (ASTM D 156), cloud point (ASTM D 2500), pour point (ASTM D 97), kinematic viscosity (ASTM D 445), and flash point (ASTM D 92). Upon arrival at Fermilab, but before accepting delivery of each railcar, a sample of the delivered oil was tested to ensure that its extinction length and light transmission curve agreed with earlier measurements made on the samples submitted during the oil selection process. Once the oil was verified to be Marcol 7 with an acceptable extinction length, it was offloaded from the railcar via clean plumbing to food grade tanker trucks that had been visually inspected for dirt or damage. A vent cover and dry air line was installed on the railcar before offloading in order to avoid contamination of the oil. Transfer from the tanker trucks to the detector also made use of clean plumbing, vent covers, and dry air to avoid contamination.

3.2 Oil Properties

Further measurements were performed on the mineral oil after its delivery to better determine its properties in order to model optical photon transport in the detector simulation. Some of these measurements are presented in Table 1.

The density and the coefficient of volume expansion were measured with a 20 ml pycnometer. The index of refraction and dispersion were measured with an Abbe Refractometer (Model WY1A, Xintian Fine Optical Instrument Corp., China) at a temperature of 20°C. The temperature dependence was also measured and is given in Table 1.

The angular distribution of Rayleigh scattering was measured at 442 and 532 nm [7]. All combinations of incident and scattered polarization with respect to the scattering plane were measured, allowing isolation of components due to isotropic and anisotropic density fluctuations. Absolute measurement of

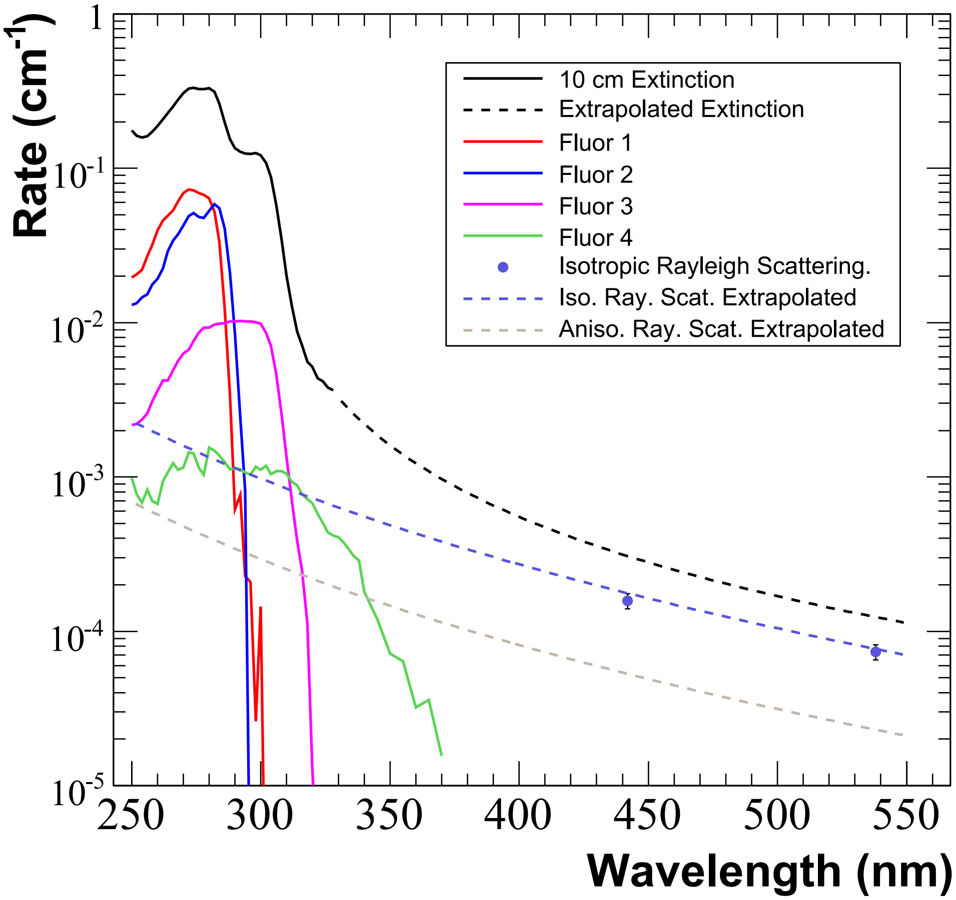

Fig. 3. Extinction rate in Marcol 7 mineral oil and some of the processes contributing to it. The solid curves and data points are laboratory measurements on small samples [7]. The dashed curves are extrapolations after empirical adjustment using MiniBooNE data. The black curves show the total extinction rate, which is measured directly. It must include the other measured processes: fluorescence (four measured fluorophores are shown), Rayleigh scattering (two measured components shown), and a small contribution from Raman scattering (not shown). The remainder of the extinction is inferred to be absorption.

the scattering rate was accomplished by comparison to the calculable Mie scattering from a suspension of 50 nm polystyrene spheres.

Both time-resolved and DC spectrofluorometer measurements were used to characterize the fluorescence of the mineral oil [7], with lifetimes and excitation and emission spectra determined for several identified fluorophores. The measured lifetimes ranged from 1 ns to 33 ns. These measurements also characterized a small rate of Raman scattering in the oil.

To obtain the light extinction function for the mineral oil, we performed several sets of measurements. At wavelengths $\lambda > 340$ nm, where the extinction length exceeds a few meters, the shape of the light transmission curve as a function of wavelength at a fixed path length and the absolute transmission of light at 460 nm as a function of path length were measured. The latter gave an extinction length of ∼25 m at 460 nm. A transmission function of both wavelength and path length was then obtained by scaling the relative, wavelength-dependent transmission curve to the absolute, path-length-dependent curve [6]. Below 340 nm, transmission through 10 cm of oil was measured in a spectrophotometer [7].

When the optical model developed from these measurements was compared to MiniBooNE data (primarily electrons from at-rest decays of cosmic ray muons), we found that the data preferred a longer extinction length than the direct measurements at the longer wavelengths, ∼40 m at 460 nm. This difference has not been resolved. The 40 m extinction length at 460 nm, combined with other parameters adjusted simultaneously, gives a good representation of MiniBooNE data and is used in our simulations. Various elements from the final optical model are shown in Fig. 3. In this model, above 400 nm the extinction is due chiefly to Rayleigh scattering; below 300 nm it is mostly due to absorption and fluorescence.

3.3 Oil compatibility

All materials in the tank (PMT's, cables, and support structures) are immersed in mineral oil, therefore it was necessary to make sure that these materials would not contaminate the oil over the duration of the experiment. The danger is that the contamination could cause changes to the optical properties of the oil that could adversely affect the performance of the detector or make it difficult to model. The materials and their potential for contaminating the mineral oil are:

- Painted surfaces: Of particular concern was the leaching of residual solvent from incompletely cured paint. Solvents contribute additional scintillating components to the mineral oil.
- Plastics: Plastic components, such as cable jackets, contain plasticizers, added to a polymer in order to produce a flexible plastic, which can be the cause of contamination that could affect the oil extinction length.
- Metals: The carbon steel tank was painted, as were the aluminum components of the phototube support structure. Nevertheless, some metal may be exposed to the oil, through pores and nicks in the paint, and because some "buried" surfaces, like the inside of metal tubing, could not be painted. It is believed that metals do not cause contamination of the mineral oil directly, but their presence acts as a catalyst for oxidation, particularly at temperatures above 60°C. Oxidation decreases the oil extinction length.

Any material proposed for use in the tank was soaked in oil, usually for at least a week and often longer, with a sample at room temperature and another at 66°C (150°F) to speed the aging process. Each sample was paired with a control that contained the same oil as the test sample, but with no potential contaminants added. The controls were drawn at the same time as the test samples and treated identically, including having the same type of container and same temperature profile. The optical properties of the oil were then measured. A spectrophotometer was used to look for changes in light transmission, and a fluorometer was used to look for changes in scintillation properties.

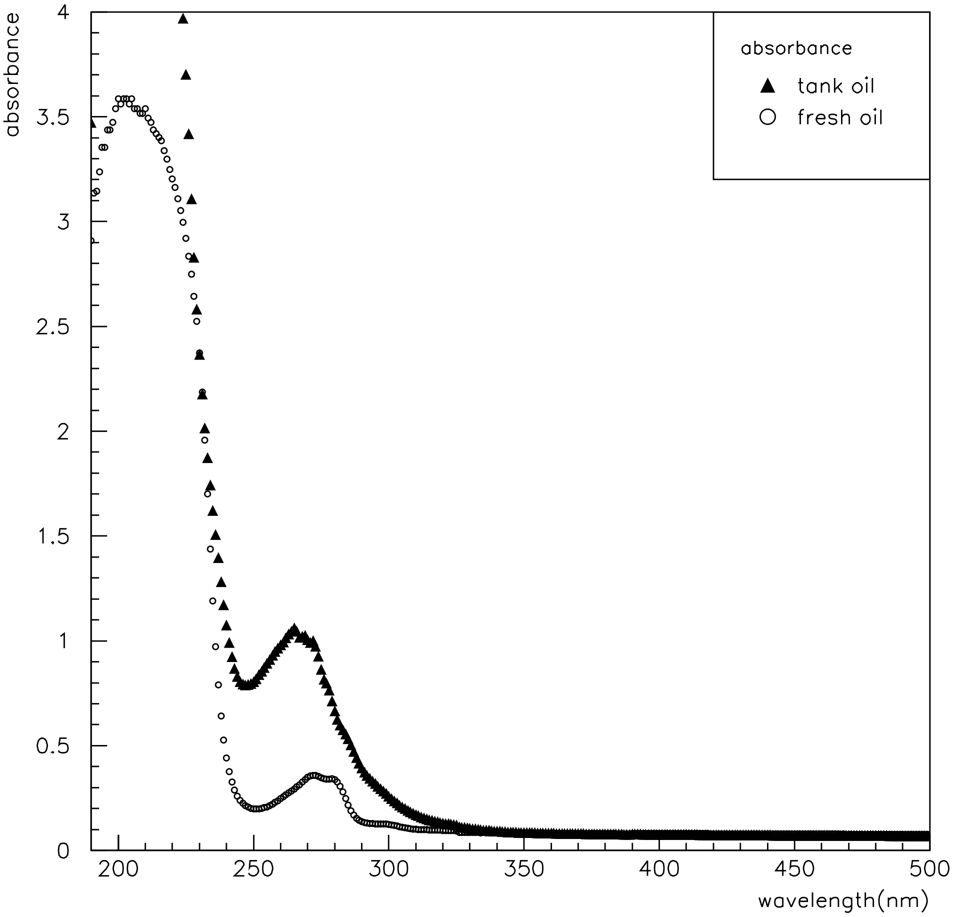

Fig. 4. Absorbance spectra of fresh mineral oil from the Witco Corporation (circles) and oil from the LSND storage tank (triangles).

As a test of our procedures, oil drawn from the LSND storage tank in 1998 was compared to newly-acquired "fresh" samples of the same Witco mineral oil. There is evidence that the black paint used in LSND caused some problems; they experienced a rising level of scintillation over their approximately six years of operation. The LSND storage tank was prepared internally in the same way as its detector tank, but the oil stored there for 6 years had no scintillator added. While fresh mineral oil is odorless, the LSND storage tank oil had

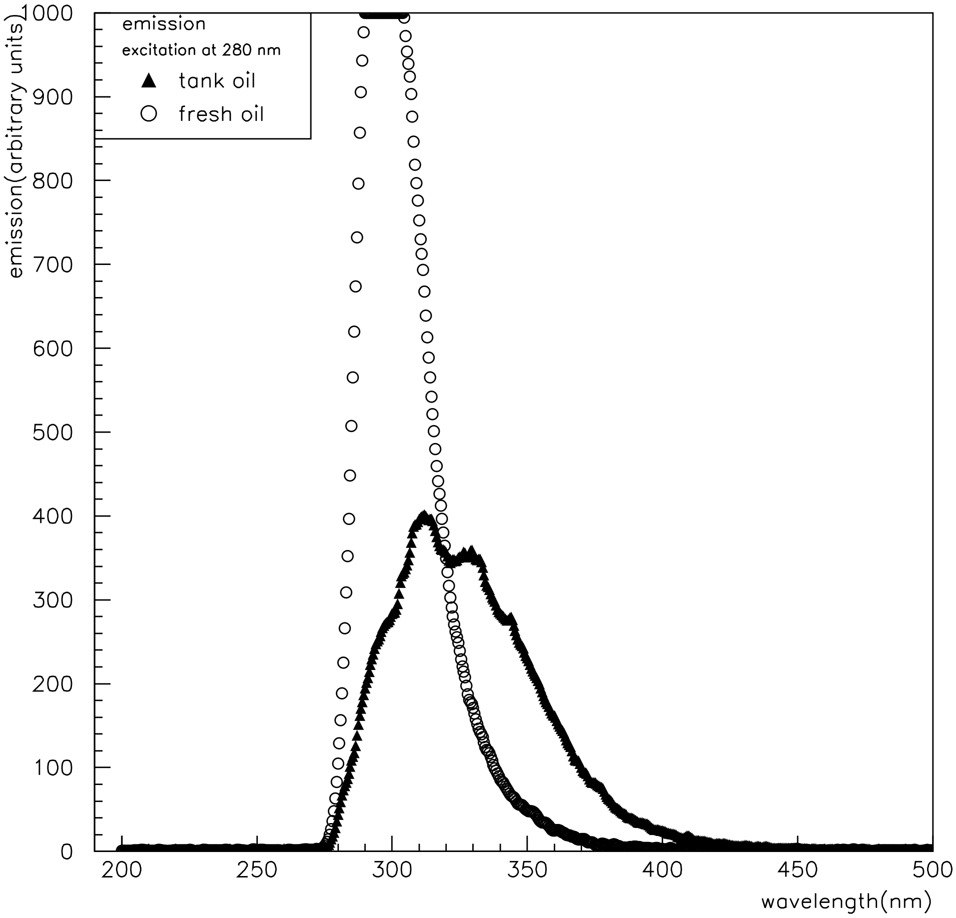

Fig. 5. Emission spectra of fresh mineral oil from the Witco Corporation (circles) and oil from the LSND storage tank (triangles). The samples have been excited at 280 nm.

the smell of paint (which was also true of the oil from the LSND detector when it was decommissioned). Figure 4 shows the absorbance in 1 cm of oil. “Absorbance” is defined as $-\log_{10} T$, where T is the transmission. Note that an absorbance of 1.0 in a 1 cm sample corresponds to an extinction length of only 4.3 mm. While we are interested in maintaining extinction lengths of many meters at wavelengths near the peak of the PMT efficiency around 400 nm, changes in the location and structure of the turn-on of strong extinction proved to be a sensitive indicator of contamination. Such an effect is clearly seen in Fig. 4. Figure 5 shows emission spectra produced from oil samples when excited by 280 nm light. The LSND storage tank oil has a significantly broader excitation spectrum. Both of these measurements indicate the presence of contaminants in the storage tank oil.

The surface coatings (the white of the veto volume and the black of the main volume) present the largest surface area of material in the oil and therefore present the greatest threat of contamination. The tank and PMT support structure coatings for MiniBooNE discussed in Sec. 4.2 were chosen from those

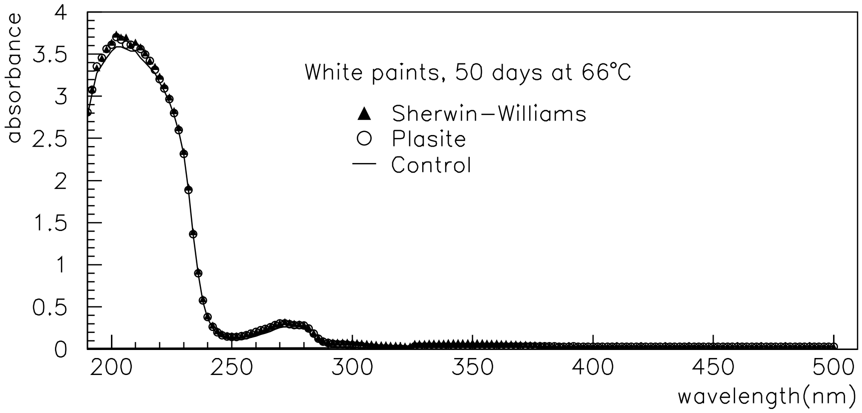

Fig. 6. Absorbance spectra for oil in which metal plates painted with the two white coatings used in the MiniBooNE tank were soaked for 50 days at 66°C. The solid line is the spectrum for the control sample of oil.

found not to change the optical properties of the oil. Figure 6 shows the absorbance results for the two white paints used in the tank.

The PMT HV/signal cables also present a large surface area to the oil. We found that PVC-jacketed cables, including the RG-58C/U with a "non-contaminating" jacket used in LSND, contaminate mineral oil. An example of these results is given in the top panel of Fig. 7, which shows absorbance for oil in which new samples of PVC-jacketed RG58 were soaked for one week at room temperature. Teflon-jacketed cables were found to be non-contaminating and Belden 88240 white (also called "snow beige") cables of this type were chosen for MiniBooNE. The bottom of Fig. 7 shows absorbance for oils in which teflon-jacketed cables soaked at 66°C. One of the samples shown was allowed to soak for over two months, with no contamination observed.

Further tests indicated that as a PVC-jacketed cable soaks, its contamination rate decreases. Figure 8 shows absorbance when the same cable shown in Fig. 7 (top) is soaked again for one week in fresh oil. Also shown in Fig. 8 is the absorbance for oil in which a cleaned sample of cable from LSND (*i.e.,* the cable was immersed in the LSND tank during the life of the experiment) soaked for one week at room temperature. The smaller impact on the oil demonstrated in this figure permitted the reuse of the short lengths of PVC-jacketed cable already attached to the bases of the PMT's recycled from LSND.

The bases and necks of the LSND phototubes were coated in Hysol potting compound. New Hysol samples and samples taken from an LSND phototube were found to contaminate oil. Therefore a new encapsulant epoxy was chosen; EP21LV from Master Bond (Hackensack, New Jersey). This epoxy meets FDA requirements for food compatibility and was found to be non-contaminating in

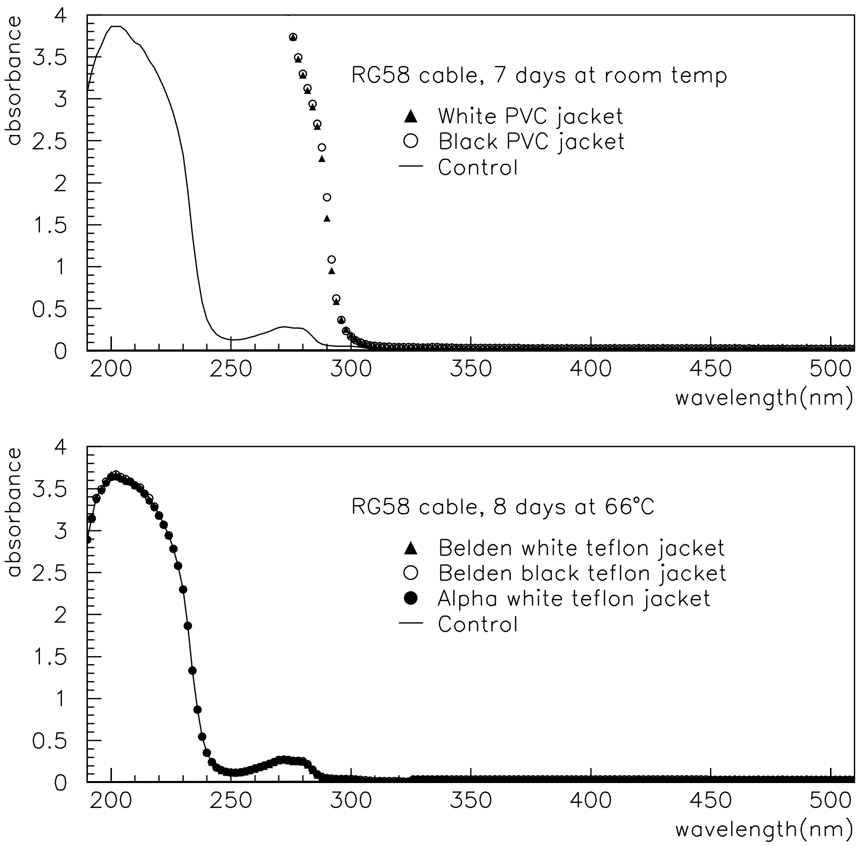

Fig. 7. Absorbance spectra for oil in which new samples of RG58 cable were soaked. Top: black and white PVC-jacketed cables soaked for 7 days at room temperature. Bottom: Black and white teflon-jacketed cables soaked for at least 8 days at 66°C. (The spectrum shown for the Belden white cable, the type ultimately used in MiniBooNE, was actually taken after an additional 69 days at varying temperatures.) The solid line is the spectrum for the control sample of oil.

our tests. Both MiniBooNE's old and new phototubes were potted in Master Bond epoxy; in the case of the old tubes, the Master Bond was applied over the Hysol.

Hundreds of samples were tested to check other components. In addition, it was confirmed that metals do not cause contamination of the oil at room temperature and that they seem to catalyze oxidation at higher temperature. Tests with aluminum and copper in oil at 66°C indicate contamination (the copper is worse), and the contamination at 66°C is much smaller when the oil samples are kept in a nitrogen environment. Therefore unpainted metal was acceptable in MiniBooNE (we have some unpainted aluminum, but no copper), where the oil remains cool and under nitrogen.

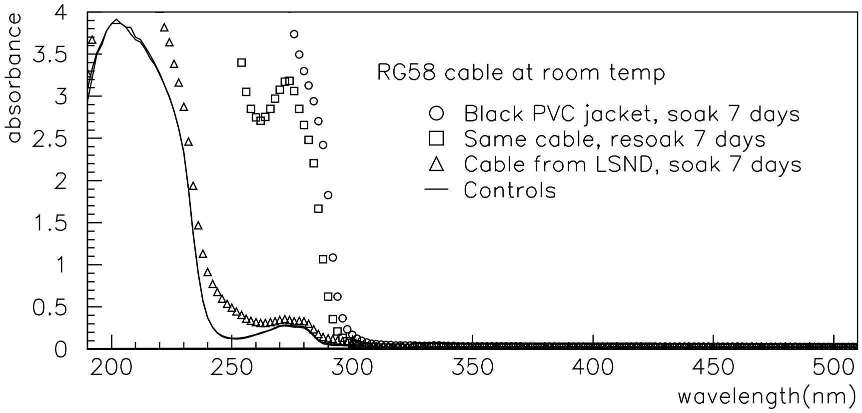

Fig. 8. Absorbance spectra for oil in which black-PVC-jacketed RG58 cable were soaked. The figure compares three samples: a new cable, soaked for 7 days (same data as the top panel of Fig. 7), the same cable resoaked in fresh oil for 7 days, and a sample of cable from LSND (i.e. a piece of cable that was immersed in the LSND tank during the duration of the LSND experiment), cleaned and soaked in fresh oil for 7 days. The solid lines are the spectra for the control samples of oil that accompanied the test samples.

4 PMT Support Structure

The photomultiplier tube support structure (PSS) includes the hardware for supporting 1280 main and 240 veto photomultiplier tubes (PMT's), the optical barrier separating the main and veto oil volumes, the fixtures for support and strain-relief of the PMT cables, and support for the various in-tank calibration and monitoring systems. The dimensions of the sections of the PSS were chosen to uniformly distribute the main PMT's over the inner surface of the optical barrier and the veto PMT's over the tank wall.

It is not possible to distribute the phototubes over a sphere with exact uniformity. For reasons of structure and ease of installation, the PMT's were deployed in evenly-spaced horizontal rows. The number of tubes in each row had to be even (since two tubes were placed on each panel of the optical barrier) and was chosen to maintain horizontal spacing that is as close to uniform and as close to the vertical spacing as possible. The odd-numbered rows started with the first tube shifted by half the horizontal spacing of the tubes in that row. Fig. 2 shows the resulting layout.

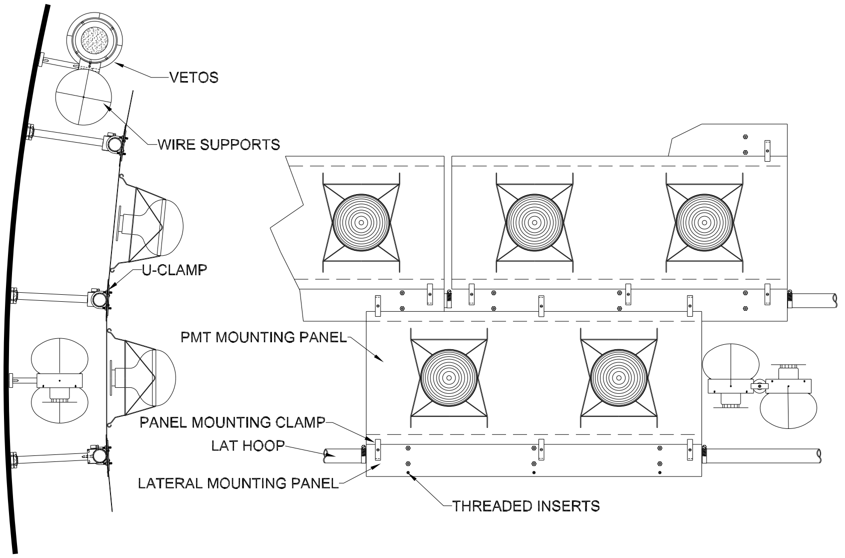

Fig. 9. Overview of the Phototube Support System.

4.1 Structure

The basic design of the support structure is shown in Fig. 9. The optical barrier panels are mounted on a set of latitudinal hoops each made of sections of 5.08 cm (2 inch) diameter, 3.2 mm ($\frac{1}{8}$ inch) wall, aluminum tubing. The sections are independently supported, but are connected by sleeves to aid alignment. Each hoop section is clamped to 2.54 cm (1 inch) diameter steel struts, which are in turn bolted to bosses welded to the tank wall. The PMT's viewing the main oil volume are mounted on the panels of the optical barrier.

Besides the obvious requirement of adequate strength, the PSS had to be straightforward to install and tolerant of deviations of the tank wall from a perfect sphere. (Industry standards limit such deviations to 1%, or about 12 cm.)

A finite-element analysis of the tank showed that, while the displacements of the tank wall when the oil was added would be, as expected, very small, differential rotation of nearby struts could magnify this effect. The largest relative displacements, about 3 mm between the free ends of adjacent struts, occurred between strut pairs that straddled the region where a tank leg joined the sphere. Because the structure's ability to handle differential horizontal motion was limited, we modified the boss layout to have bosses centered horizontally on each leg, reducing the maximum relative horizontal displacement to less than 0.5 mm.

After the tank was complete and the bosses welded on, the Fermilab Alignment Group surveyed the boss locations. The survey indicated radial excursions on the order of 2 cm in the tank wall. We fabricated the struts in 0.64 cm ($\frac{1}{4}$ inch) increments in length, with each boss assigned a strut length based on the survey. The base of each strut is a disk with a recessed ball-bearing at the center. This provides a pivot point, and the relative tightening of the three mounting bolts could move the other end of the strut by about an inch in any direction. This provided further compensation for irregularities in the tank wall and allowed generous tolerances in the placement of the bosses on the tank wall, minimizing the cost of their installation.

The panels of the optical barrier were made from 1.6 mm ($\frac{1}{16}$ inch) aluminum sheet. Each panel is approximately 1.2 m wide by 0.6 m high and holds two PMT's. Experience with a full-scale prototype of a section of the PSS indicated that flat panels easily conformed to the supporting hoops, so that rolling them to the correct curvature was not necessary. When mounted, each row of panels formed a section of a cone, with the whole optical barrier approximating a sphere. (The sagitta formed by comparing the cones to the sphere is 0.7 cm.) The panels were not mounted directly to the hoops. Instead, they mounted to 15 cm wide strips which in turn mounted to the hoops using U-bolts. The panels were attached to the strips by clips. The lower clips clamped the panels to the strips, while the upper clips captured the panels without clamping them. Gaps of about 2 cm were left between adjacent strips and panels in the same rows. These gaps were blocked by narrow aluminum strips, pop-riveted to the strip or panel on one side. This arrangement has a number of virtues:

- The overlap provides a robust optical barrier. With the detector complete, measurements with the central laser flask showed the leakage of light to be $< 10^{-3}$.
- Variable gaps between panels horizontally and vertically allowed loose mechanical tolerances, easing installation.
- The use of the strips and clips decoupled the horizontal positions of panels in adjacent rows. This and the gaps meant that installation variations did not accumulate as rows were added.
- The fact that the panels were clamped only along one edge (and, similarly, the inserts connecting the latitudinal hoop sections were only fastened on one end) allowed the structure to shift slightly after installation, as could happen when the 800 tonnes of oil was added or from thermal expansion.

To ensure uniform distribution of the oil during filling and circulation, there are several ports through the optical barrier. These are equipped with baffles to prevent light from crossing the barrier.

Two PMT's were mounted to each panel using the existing PMT mounts from LSND (see Fig. 10), plus some new ones made to the same specifications. The stands are made of 2.54 mm (0.1 inch) stainless steel wire and an equatorial band of stainless steel sheet 1.27 cm (0.5 inch) wide and 1.6 mm (0.065 inch)

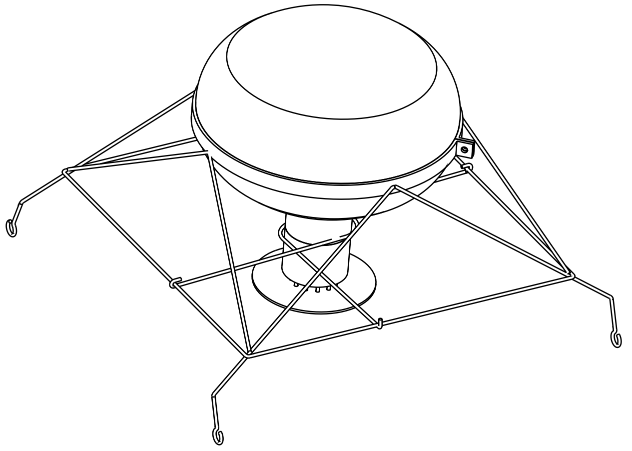

Fig. 10. 8-inch photomultiplier tube in LSND stand.

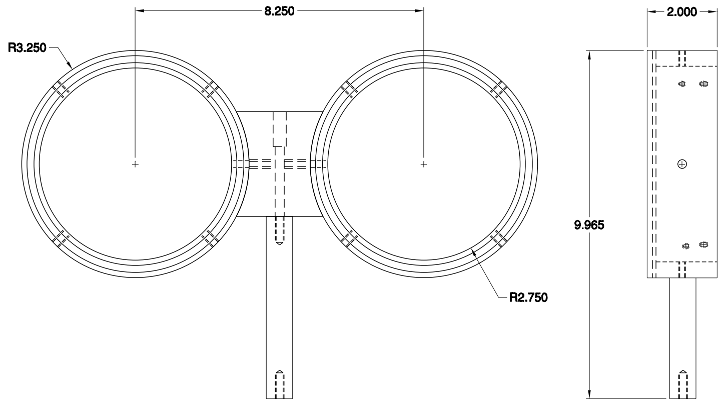

Fig. 11. Veto PMT cluster. The strut mounts to a boss welded to the tank wall. The PMT's sit in the rings. Dimensions are in inches.

thick. The new PMT's differ from the old ones in the diameter of the neck, so new centering clips were produced to accommodate them. The stands attached to blocks mounted on the panels.

The veto PMT's were mounted in opposite-facing pairs on struts attached to bosses welded to the tank wall. The mounting scheme is shown in Fig. 11. Each phototube rests on a viton o-ring which in turn sits on a step in the end of an aluminum pipe. A cross of stainless steel wire captures the globe of the tube against the o-ring, while nylon screws center the neck of the tube in the pipe. The orientation of each cluster on its strut could be varied to avoid obstructions. Monte Carlo studies showed no differences in average light collection among various possible patterns in the orientation.

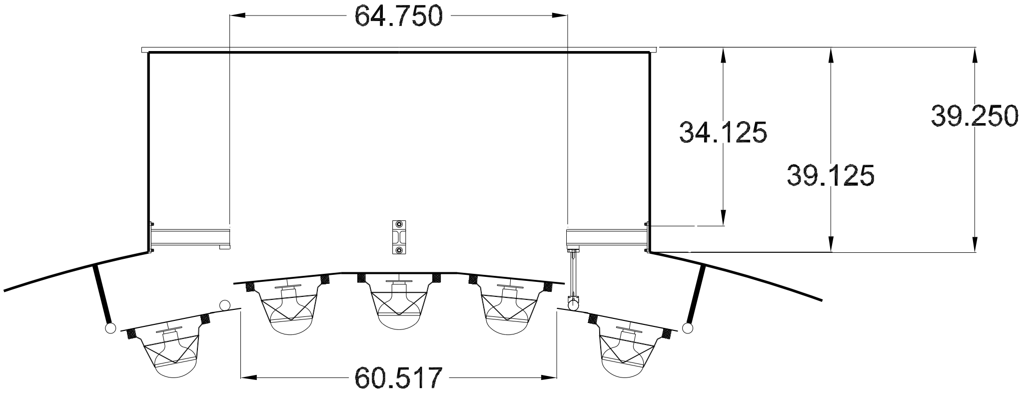

Fig. 12. The top polar cap. Dimensions shown in inches.

Part	Total weight (metric tons)
panels/strips	2.1
lat hoops	0.9
bosses/struts	1.0
hardware	0.05
PMT's/bases	1.5
LSND stands	0.3
cables (in tank)	0.7
Total	6.6

Table 2
Total weight, in metric tons, of various PSS components.

To facilitate installation, the top and bottom "polar caps" were treated specially. Each holds the polar PMT and the next row of 6 PMT's. The top cap also holds the scintillator cubes of the calibration system (see Sec. 7.2). Fig. 12 shows how the top polar cap was mounted. For uniform light collection in this region, a white aluminum panel was mounted on the I-beams shown in the figure, just under the surface of the oil in the top access portal. The top veto PMT cluster was also mounted from these I-beams.

The main PMT's are about 55 cm apart; the veto tubes are about 2 m apart. A survey taken with the tubes in place showed the average radial location of the apex (innermost point) of the main-tank tubes to be 548.2 cm, consistent with the dimensions of the mounting hardware.

Table 2 shows the weight of various PSS components. These can be compared to the approximately 37 metric tons of the tank shell itself, the approximately

800 metric tons of oil, and the total buoyant force of the PMT's in oil of 4.6 metric tons.

4.2 Surface finishes

Surfaces of the detector were painted to provide high albedo in the veto volume and low albedo in the main volume. Reflection of light in the main volume of the detector can cause Cherenkov light to appear isotropic and delayed, degrading particle identification. We thus wanted surfaces in the main volume to be non-reflective. In the veto volume, we simply wanted to maximize the total light collected by the sparse array of PMT's. The inner surface of the tank wall, the bosses, the struts, the latitudinal hoops, and the outer side of the panels, strips, and overlaps of the optical barrier were painted white. The inner side of the optical barrier was painted black. Small parts on the inner surface of the optical barrier, such as the clips and PMT mounting blocks, were black-anodized.

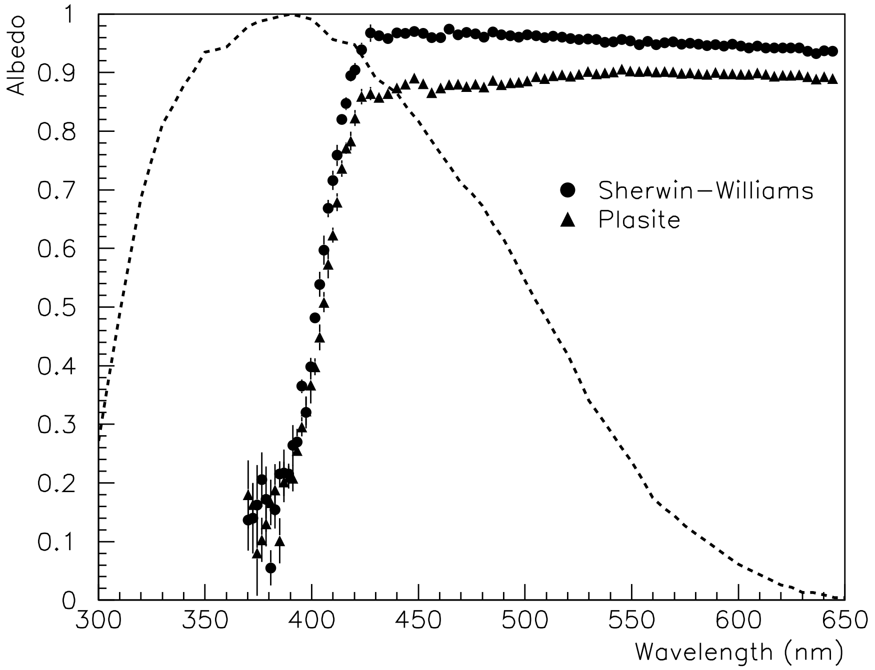

Fig. 13. Albedo measurements for the white coatings used in the tank. For reference, the dashed curve shows the PMT quantum efficiency, normalized to its maximum value [4].

We measured the albedos of various paints in air using a tungsten lamp and integrating sphere. All of the measured white coatings provided better than 80%

albedo at wavelengths above 425 nm, and Fig. 13 presents the measurements for the chosen white paints. We also measured albedos in oil by immersing a sample, a light source (an alpha emitter embedded in scintillator), and a detecting PMT. These in-oil measurements confirmed our rankings of candidate surface treatments.

The steel tank was painted after construction with Plasite 9060, a white epoxy coating. Plasite Protective Coatings (Green Bay, Wisconsin) markets this tank lining to the food and beverage industries, saying that it will not impart taste or odor, and that it meets FDA requirements for direct food contact. Our own tests indicated that it does not contaminate mineral oil (see Sec. 3.3).

The components of the phototube support structure were painted with coatings manufactured by Sherwin-Williams (S-W). We found that these coatings were non-contaminating. In albedo tests of samples gathered from various manufacturers, the S-W white offered the highest albedos, whereas the S-W black offered the lowest. The white is an aircraft paint (F91W26/V93V28/V93V2 Jet Glo Gloss Polyurethane White) and the flat black is a military paint (F93B102 Flat Black Moisture Cure Polyurethane). Both were applied over a primer (E72AC500/V66V503 Hydralon P Waterbased Epoxy Primer (Grey)).

Some of the smaller pieces of the PSS (panel clips, the blocks to which the PMT stands attach, calibration cubes) were black anodized. This process was shown to be non-contaminating, and is a fast, cost-effective way to finish a large number of small pieces. However, a smooth black anodized aluminum surface offers fairly high albedo at large incidence angles; to achieve lower albedo the surface must be scuffed (e.g., sandblasted) prior to anodizing. Anodizing was considered for the panels and rejected because of the need for low albedo over the full range of incidence angles and the concern that sandblasting might curl the panels. The smaller pieces were deburred in a tumbler, which left them slightly scuffed, making them ideal candidates for anodizing.

4.3 Installation

The installation of the PSS began in January 2001 and was completed in October 2001. Installation was done from scaffolding supplied and installed by Bartlett Services, Inc., consisting of six levels with an internal stairwell.

With the scaffolding in the tank, the cable bundles were installed in their flanges. PSS/PMT installation then began on the top scaffold level with the PMT row below the top polar cap. Each scaffold level was lowered or removed as the PSS and PMT's above that level were installed and tested to allow access further down the tank wall. The first steps at each level involved installing the latitudinal hoops to the desired height using a rotating-laser level that traced a horizontal line around the tank. The height reference was a steel measuring tape hanging from the top access portal. It was calibrated by using the laser level to transfer the surveyed coordinates of many bosses to the tape.

At regular intervals, the tank ports were closed and the installed PMT's and cabling were tested at high voltage using a temporarily-installed LED flasher system.

When nearly all the PMT's were installed, the Fermilab Alignment Group surveyed the positions of about 40% of the main tank tubes. The survey showed that the horizontal rows had an rms deviation from the desired polar angle of 0.08 degrees, corresponding to 0.7 cm at the radial location of the tubes. The rms polar angle of the individual tubes within a row was of the same order. Horizontally, the rows were oriented to within typically 0.25 degrees of the desired azimuthal angle, corresponding to about 2 cm. The radial position of the tubes had an rms of 0.9 cm.

5 Utilities

5.1 Cable Plant

The tank cable run links the photomultiplier tubes to the preamplifiers, located in crates in the tank access area next to the top tank access port. A single RG-58 cable both supplies high voltage to a PMT and carries the signal from PMT to preamp. As described in Sec. 3.3, teflon-jacketed cable, Belden 88240, is used for compatibility with the mineral oil. This cable has the further advantage of being plenum-rated. It is thus suited for running under the computer floor to the preamps. As most of the run is in the veto section of the tank, cable with a white jacket is used. The cable terminates at the preamp end in a SHV jack.

The penetration of the tank wall is through airtight feedthroughs bolted to the flange on the tank access portal. The oil level in the access portal remains below these flanges; the seal is to maintain the nitrogen atmosphere in the tank. Each flange accepts eight bundles of 49 cables.

To maintain uniformity in pulse shape from tube to tube, cables of a fixed length, 30.5 m (100 ft), were used for all channels, despite the disparity in the length of the cable runs to the top and bottom of the tank. Each cable is captured in the feedthrough with only the length necessary to reach the PMT extending from the inner side.

Each cable bundle serves the main and veto PMT's in a vertical slice of the tank from top to bottom. Cables for the main PMT's cross the veto region and penetrate the optical barrier through pairs of holes near the center of each panel. After passing through the optical barrier, the cable was spliced to the 1.5 m length of black-jacketed cable that is permanently attached to the PMT base. The splice was made with a coaxial splice kit (Raychem B-202-81, formerly D-150-0071). This system was used in LSND and found to be very reliable. Of the 13 PMT failures that occurred in the first five years of MiniBooNE running, two or fewer were attributable to splice failures. To seal out oil, the splice was covered with a length of 9.5 mm ($\frac{3}{8}$ inch) teflon shrinktube (SPC Technology SST-024), which shrunk onto viton o-rings on either side of the splice.

As each splice was made, it was tested. Prior to splicing, a pulser was connected to the cable at the preamp end and the reflection (at about 370 ns) was observed on an oscilloscope. Since the bases are back-terminated, the disappearance of the reflection after splicing indicated both that the splice was good and that the labels at the two ends of the cable matched.

Upon exiting the tank flange the cables were then routed under the raised floor system surrounding the access portal to the preamplifiers. Prior to preamplification, the PMT signals from single photoelectrons are small. The raised floor between the tank access portal and the preamplifiers was thus lined with copper mesh forming a Faraday cage to provide additional shielding from noise pickup.

5.2 Oil Plumbing

The MiniBooNE detector oil plumbing system was designed to enable filling, recirculation, filtering, temperature control, and removal of the the mineral oil. A schematic of the oil plumbing system for the MiniBooNE detector is shown together with the N_2 system in Fig. 14. All components of the system are food-grade and all oil pipes are stainless steel. Oil enters the detector tank (capacity 950,000 liters) during fill or recirculation via a 7.62 cm (3 inch) pipe that attaches to the inflow penetration at the bottom of the detector tank. During decommissioning of the detector, this line will be used, together with a pump located in the bottom of the detector vault, to remove the oil.

Flow studies indicated that, unless oil was supplied directly to the main volume of the tank, most of the circulation would be through the outer (veto) region. For this reason, oil enters the tank through a coaxial, light-baffled, fitting that delivers most of the oil to the main volume. Another 7.62 cm (3 inch) pipe is attached to the outflow flange on the detector tank access portal. This

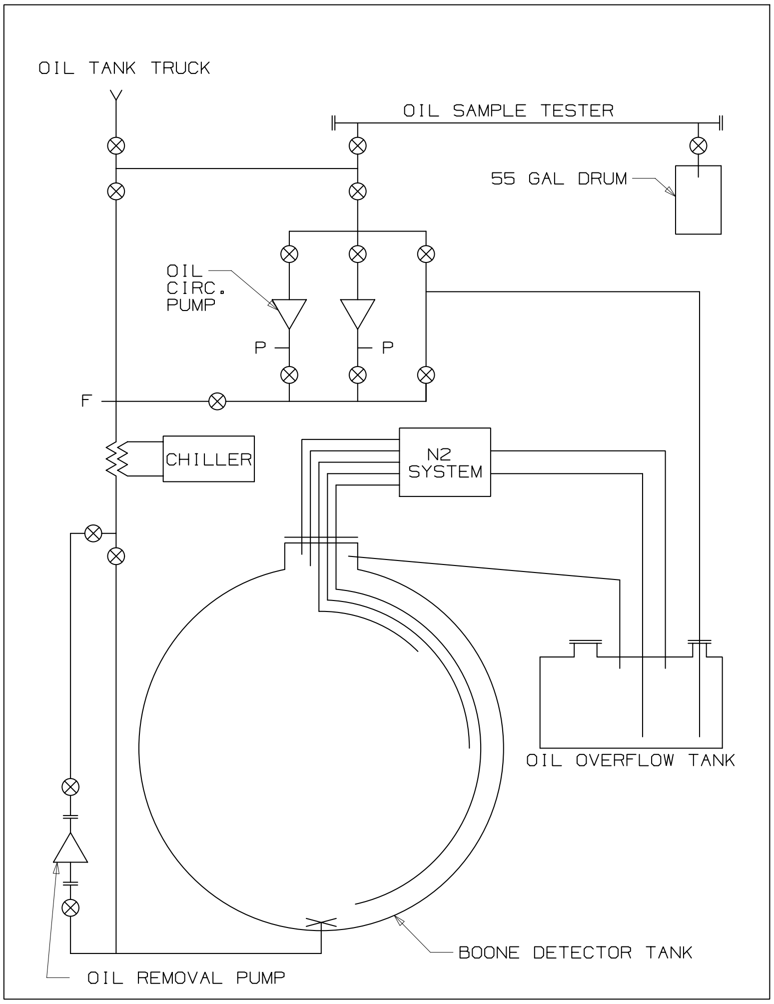

Fig. 14. A schematic figure of the MiniBooNE detector oil plumbing and N_2 systems.

outflow line is routed to the oil overflow tank with a 1% slope so that any oil pushed out from the detector tank will passively flow to the overflow tank. The outflow line is attached to the access portal below the level of the PMT cable ports so that the maximum height of oil is maintained at a level below any other penetrations into the tank.

A 9,500-liter stainless steel oil overflow tank is located beneath the detector entrance hall and provides an overflow capacity of 1% of the detector tank volume. The thermal expansion coefficient of the mineral oil was measured to be 6.1×10^{-4} °C^{-1}, therefore, the tank allows an oil temperature change of 16° C, well within any expected temperature variation.

During the filling stage, oil was pumped from the stainless steel tanker truck into the bottom of the detector via the fill line. A stainless steel filter installed in the inlet line removed most of the particulate matter as oil was pumped in during delivery and during the later recirculation phase. The detector main tank was completely filled and the overflow tank was filled to a third of its capacity.

The oil inflow line passes through a heat exchange unit attached to a chiller with 10 kW capacity. This arrangement allowed for cooling the oil during the initial oil fill as well as during standard running in order to help remove the approximately 600 W of heat generated by the PMT's. However, the temperature of the oil during fill and subsequently, during standard operation running, has not necessitated the use of this chiller.

5.3 Nitrogen System

The amount of emitted scintillation light and the light attenuation in the detector oil can vary strongly depending on the amount of oxygen dissolved in the mineral oil. Therefore, to maintain a stable detector medium, a nitrogen environment is maintained throughout the oil plumbing system. In addition, the (dry) nitrogen keeps water out of the detector tanks and lines and reduces the problem of oxidation on exposed metal surfaces.

The nitrogen system is shown schematically in Fig. 14 and consists of a 1000 liter dewar of liquid nitrogen that provides gaseous N_2 via boiloff at 17 psi. The gas is routed to 2 microbubble (Point Four MBD600) diffusers located at the bottom of the overflow tank. Nitrogen is also provided to one open line at the top of the overflow tank and four open lines terminating at various heights within the detector tank. Return lines were installed at the top of the detector and overflow tanks and vented outside of the detector hall.

Upon delivery, gas analysis indicated that there were approximately 30 (atmospheric) cubic meters of oxygen dissolved within the mineral oil. In order to reduce this, 30 (atmospheric) liters per minute of N_2 was routed to the microbubble diffusers in the overflow tank while the mineral oil was recirculated through the overflow and detector tanks at 80 liters per minute. This situation was maintained for one month. A total of about 1 million atmospheric liters of N_2 was bubbled through the detector oil in order to reduce the oxygen concentration by a factor of 10.

After this procedure, the vigorous N_2 flow to the microbubble diffusers was stopped and the oil recirculation halted. Since that time, oil has not been recirculated through the system and the N_2 flow has been set to approximately 1 liter per minute through the open lines to maintain the N_2 environment in the tank.

5.4 *Detector Environmental Monitoring*

A detector environmental monitoring system was installed to measure various quantities during the commissioning and run phase of the experiment. These include: air temperatures and relative humidities in the detector enclosure and within the electronics racks; temperature, level, and flow rate of the detector mineral oil; and pressure and flow rate of the N_2 gas. These quantities are measured at multiple locations throughout the detector and enclosure. This system employed various commercial probes, displayed the values on panel gauges, digitized the data using a standalone ethernet data acquisition device (wedDAQ/100), and archived the values.

The average air temperature is 21° C in the upper detector hall and 18° C in the lower detector vault. These values are stable to within 2° C throughout the year due to a HVAC system and the large thermal mass of the concrete structure and earth overburden. The relative humidity in these areas varies between 30% and 60% throughout the year. The exhaust air temperature in the electronics racks is monitored closely as a loss of cooling can lead to electronics failures. These probes are used with an interlock system to shut down the power to the readout electronics if the temperature rises above 40° C. The temperature of the mineral oil is quite stable without additional cooling and is monitored at three locations within the detector tank. The average temperature of the detector oil is approximately 18° C and varies by 1° C from the top to the bottom of the detector tank and by 2° C over the year.

The oil level in the detector and overflow tanks are monitored with capacitive level probes (Kubold NRF series). In the detector tank, the probe is located to detect only the top 1 m of oil level. During the fill stage, the oil level was determined by the pressure in the N_2 lines within the tank. During the oil recirculation stage, the oil level in the main tank was set by the outlet pipe. When oil recirculation was halted, the oil level dropped slightly and varied with temperature throughout the year by approximately 20 cm. This does not affect the operation of the detector as the outer veto volume is approximately 60 cm below the maximum oil level.

6 Electronics and Data Acquisition

6.1 *High Voltage and Preamplifier System*

The PMT bases implement either a nine (old PMT) or ten (new PMT) stage design using a Hamamatsu recommended voltage taper along the dynode chain for maximal gain and reasonable linearity in the 1 to 100 photoelectron range of illumination. To remain compatible with the preamplification and high voltage (HV) distribution system, the total base resistance is kept close to 17 MOhms. The voltage divider chain is made with carbon film, 0.5 W resistors and ceramic disk capacitors and is entirely passive. The anode circuit is back terminated at 50 Ohms and is balanced to compensate for distortion caused by the capacitive coupling in the termination circuit. The base is designed to operate with positive high voltage applied to the anode. The cathode is at ground potential, and isolated from the support frame to avoid ground loops.

Each HV/Preamp board handles the high voltage distribution and preamplification of 24 PMT's. High voltage is distributed to each of the PMT's via 50 Ohm, equal length, Teflon jacketed, 3000 V rated cables which also carry the PMT signal (see Sec. 5.1). In order to achieve a uniform gain, the PMT's were sorted into groups of 24 according to their gain's dependence on voltage. An optimal voltage is then applied separately to each group, and trimmed for each channel with a fixed resistor chosen to give that channel its desired operating voltage.

The PMT signals are AC decoupled with a 0.01 μF, 3000 V, ceramic, HV capacitor and are then amplified by a factor of 20 with an AD9617 op-amp in non-inverting external feedback mode. To achieve low noise, this amplification is done in a Faraday cage and as close as possible to where the HV cables exit the tank. The amplified signals from the HV/preamp boards are carried by equal length, 50 Ohm, coaxial cable to the rear of the 8-channel DAQ charge and time (QT) boards. The racks housing the HV/preamp boards are located at least 3 m away from the data acquisition electronics so as to mitigate digital noise effects.

6.2 Signal Processing

The electronics digitizing system was designed to collect charge from each PMT, digitize the time and charge amplitudes, store these for a substantial period, and read them out when an external or internal trigger is received.

MiniBooNE re-used the LSND PMT electronics [8]. All power supplies, crates, electronic cards, and cables were checked and refurbished before installation at Fermilab.

The data acquisition electronics are housed in a total of fourteen VME crates: ten 9U QT crates process the 1280 tank PMT's, two 9U QT crates process the 240 veto PMT's, and the trigger is housed in a 6U crate. One 9U QT crate is used for high resolution time inputs from the calibration systems (see

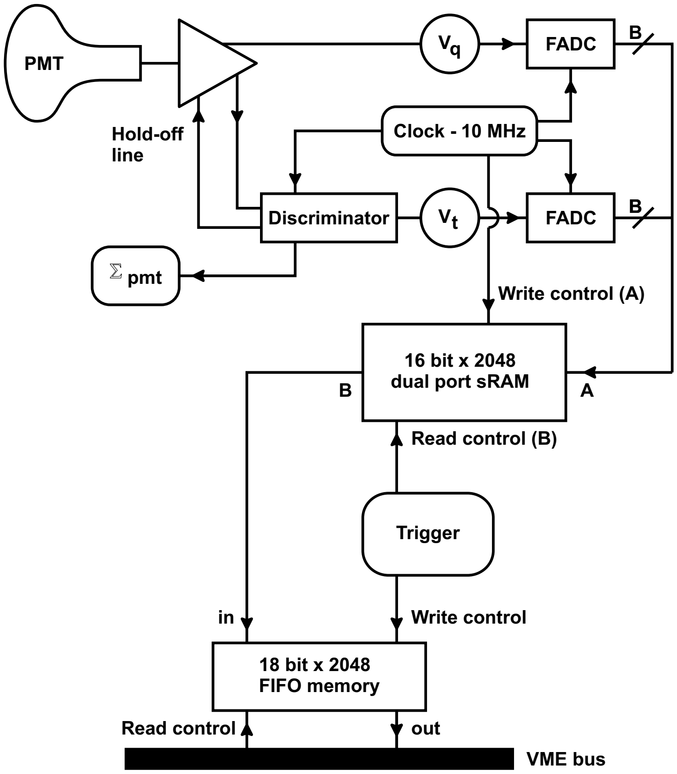

Fig. 15. A channel level block diagram of the front end QT electronics.

Sec. 7) and beam monitoring devices. All crates conform to the VME standard "A24:D32 Standard Non-privileged Data Access".

The system is driven by a 10 MHz rack-mounted GPS-disciplined clock, that feeds into the trigger crate and is distributed to the other VME crates via equal-length twisted pair ECL cables. Central to data processing is the fact that all digital information is stored on local channel memory that is addressed by the lowest 11 bits of the GPS clock. This Time Stamp Address (TSA) is distributed via the TSA bus that daisy chains all crates together, thereby keeping all hit information synchronized.

The charge (q) and time (t) information from each PMT is processed on eight-channel QT cards, of which there are sixteen in each crate. A channel level block diagram of this system is shown in Fig. 15. If a PMT registers $q > 2$ mV, a leading edge comparator discriminator fires immediately (asynchronous to the clock) registering a hit and generating a 200 ns hold-off gate synchronized to the clock. The PMT base resistor and gain are set such that 2 mV corresponds to $\sim$0.1 photoelectrons.

Figure 16 illustrates the signals produced by the QT cards in response to a PMT signal. The PMT anode pulse is connected to an integrator-stretcher circuit that convolves it with an exponential with a decay constant of $\sim$700 ns. The digitized value of this stretched voltage at each 10 MHz clock tick is the q

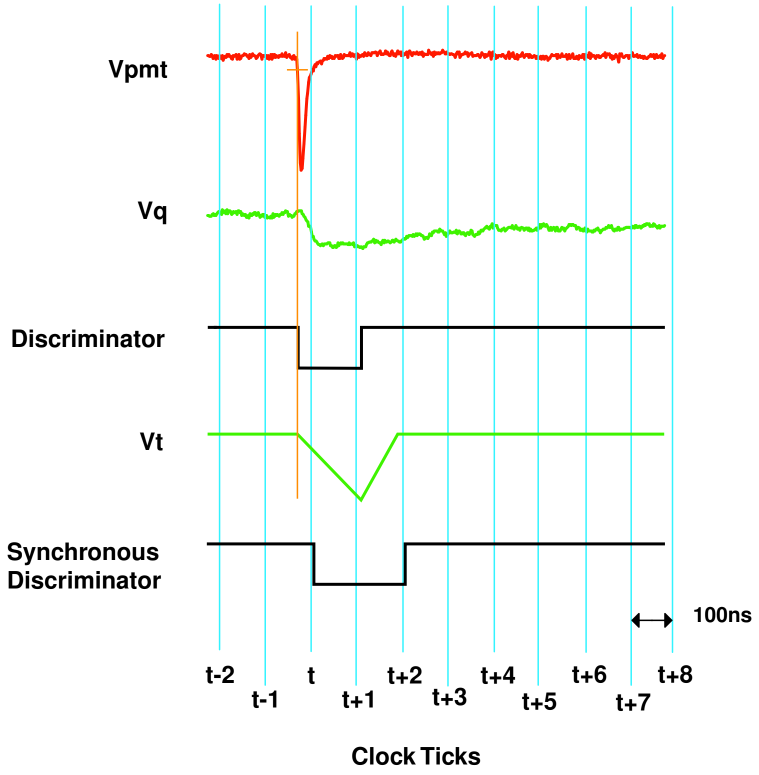

Fig. 16. MiniBooNE electronics traces and gates for a single channel which show how a PMT hit is processed by the electronics. The top trace (V_{PMT}) shows the signal of a PMT hit crossing the 2 mV threshold, with the integral (V_Q) of the pulse in the next trace. V_Q will bleed off over ∼1 μs. Next, the discriminator gate responds to V_{PMT} crossing threshold, begins the time ramp, V_T, and signals the synchronous discriminator to fire on the next available clock pulse. ADC's digitize the integrated charge (V_Q) and time (V_T) traces on every 100 ns clock tick.

measurement. The empirical shapes of the integrated charge bleed-off curves are extracted from MiniBooNE data, one for LSND PMT's and one for new PMT's. The single photoelectron resolution is approximately 4 bits, with a full scale of 20-30 photoelectrons. The time measurement is obtained by using a fixed transistor ramp circuit initiated by the asynchronous discriminator firing that quickly returns to baseline after two subsequent clock ticks. The ramp voltage, digitized at each 10 MHz clock tick, gives the t measurement. Two successive t measurements determine the voltage time slope. This is then extrapolated to the baseline voltage and gives the fine time relative to the nearest 10 MHz clock tick. It has a least count of 0.8 ns. The charge and time baseline distortions are less than 0.5% during normal running. The delay before the discriminator for a given PMT can fire again is set by the synchronous discriminator and is between 200 ns and 300 ns depending on the phase of the initial hit relative to the 10 MHz clock.

The digitization is done synchronously with the 10 MHz clock by 8-bit flash ADC's. The q and t ADC values are stored in a 204.8 μs (2048 entries spaced

100 ns apart), circular, dual-port buffer indexed by the TSA of each clock tick. Dual-port refers to the ability of the buffer to process input and output values simultaneously on each clock tick. The ADC digitization operates independently of the trigger, and the circular buffer allows just over 200 μs for the trigger to respond to the stored charge and time data before it is overwritten. During normal running, the data loss rate is less than 0.1%. The number of hit PMT's (fired discriminators) is summed on each clock tick for each crate and broadcast to the central trigger where a detector sum is done separately for both main tank and veto PMT's.

6.3 Trigger System

The MiniBooNE trigger logic is constructed in software using external information from the accelerator and calibration systems together with detector PMT multiplicity information. The software runs on a monoboard computer housed in a VME crate that also contains the (custom-built) trigger electronics modules [8]. The information used for triggering decisions is obtained from these modules.

Two trigger sum cards collect main and veto PMT multiplicity information from Σ_{PMT} cards that reside in each QT crate. The Σ_{PMT} cards compute the digital sum of the number of hits on the crate and transmit that sum on a flat ECL cable to one of the trigger sum cards, one for main tank PMT's and one for veto PMT's. The trigger sum cards then form global PMT multiplicities and pass that information to the trigger memory card where seven different, jumper-set, comparator levels (five for main, two for veto) are tested. The trigger memory card also accepts three external inputs for NIM signals which are used to input accelerator and calibration trigger signals. These external signals were "multiplexed" to allow multiple different trigger types to be transmitted on the same input. This is possible by encoding the trigger type information in the NIM pulse length. (See Table 3 for a complete list of trigger inputs.)

When any of the external input bits are set or the comparator bits indicate some activity in the detector (tank hits$\geq$10 or veto hits$\geq$6), an entry containing the states of all these bits is placed onto the trigger FIFO register (2048 words deep), along with a 16-bit time-stamp. FIFO status bits notify the software running on the trigger monoboard computer when the FIFO has data ready to process. The rate of trigger FIFO loads is approximately 150 kHz. The external input and comparator bits, along with their time history are used by the trigger software to determine if a trigger should be set.

When the software determines that a trigger has occurred, a contiguous string of TSA's, corresponding to the time window of interest, is built and written

Input	PMT Hits	Purpose
External 1	n/a	Beam to MiniBooNE
External 2	n/a	Strobe, NuMI, Debuncher
External 3	n/a	Calibration event
Comparator 1	Tanks hits$\geq$10	Activity Monitor
Comparator 2	Tanks hits$\geq$24	Michel electron
Comparator 3	Tanks hits$\geq$200	High-Energy Neutrino
Comparator 4	Tanks hits$\geq$100	Neutrino candidate
Comparator 5	Tanks hits$\geq$60	Supernova ν candidate
Comparator 6	Veto hits$\geq$6	Cosmic Veto
Comparator 7	Veto hits$\geq$4	Cosmic Activity

Table 3
The MiniBooNE external trigger inputs and comparator settings.

to the trigger broadcast card which then transmits that sequence of TSA's to the QT crates. The number of TSA's in the string varies according to the type of trigger. Receiver cards in the QT crates distribute the TSA list to the QT cards which initiates a transfer of data from dual-port memory into the QT FIFO's. As described in Sec. 6.2, the depth of the dual-port RAM allows for 205 μs of data buffering while the triggering decision is made. If that time is exceeded, the event is flagged in the data stream. The trigger hardware settings and software code was tuned to so that this loss rate was less than 0.1% during normal running.

The principal physics trigger for this experiment requires only that beam was sent to the MiniBooNE target regardless of whether or not there was any activity in the detector. This information is obtained from the accelerator clock signals via the Fermilab ACNET (Accelerator Network). This signal is routed to the trigger memory card on a dedicated input which was not multiplexed. When a beam trigger is set, a string of 192 contiguous TSA's (19.2 μs) is broadcast to the QT cards. This time window was adjusted to begin approximately 5 μs before the arrival of the 1.6 μs beam spill. In this way, activity in the detector before and after the beam spill is recorded with minimum bias. A beam trigger initiates a beam holdoff window (in the trigger software) that inhibits the acceptance of subsequent triggers for 20 μs.

Other trigger types were formed in order to produce special purpose data sets. These included triggers that were used to collect neutrino events from other sources at Fermilab (NuMI and the debuncher), to search for Supernova neutrinos, to provide calibration samples, and to monitor detector performance. These trigger types are summarized in Table 4. The total trigger rate

Trigger	Rate (Hz)	Prescale	Time Window (μs)
Beam	2-5	1	19.2
Beam γ	~0.1	1	3.2
Beam β	~0.3	1	3.2
Strobe	2.0	1	19.2
Strobe γ	0.1	1	3.2
Strobe β	0.3	1	3.2
NuMI	0.5	1	19.2
BigNu	0.66	1	19.2
Michel	1.2	600	19.2
Supernova	9.9	1	3.2
Tank	0.4	90000	19.2
Veto	0.4	5000	19.2
Laser	3.33	1	9.6
Fake beam	~0.5	1	9.6
Cube	1.1	1	12.8
Tracker	0.7	170	12.8

Table 4
MiniBooNE trigger types. The total trigger rate is ~26 Hz.

is ~26 Hz, of which up to 5 Hz is due to beam triggers. The remainder of this section describes the conditions required for and the purpose of each trigger type.

- **Beam**: The primary physics trigger for the experiment. Requires the “beam to MiniBooNE” signal from the accelerator clock and does not depend on PMT activity in the detector.
- **Strobe**: Generated by a pulser running at 2 Hz, this trigger produces an unbiased sample of beam-off triggers for background studies.
- **NuMI**: Set via the accelerator clock signal for beam sent from the Main Injector to the NuMI beamline. It is analogous to the Beam trigger and allows MiniBooNE to detect off-axis neutrinos from the NuMI target [9]. The Fermilab accelerator clock cycles are such that this trigger does not overlap with MiniBooNE Beam triggers.
- **BigNu**: Requires tank hits $\geq$200 and veto hits <6 and occurs outside the beam and laser time windows. This trigger is set for neutrino candidate events that are not induced by the Booster or NuMI neutrino beams.
- **Michel**: Requires tank hits <200 and veto hits <6 and the signature of a

cosmic-ray muon (tank hits $\geq$100 and veto hits $\geq$6) between 3 and 15 μs prior. The trigger collects a sample of cosmic-ray muon-decay electrons ("Michels") in the detector. The total rate of muon-decay electrons in the detector was approximately 2 kHz, the requirement on a previous muon signal and prescaling reduced the rate of this trigger to 1.2Hz.

- **Supernova**: Requires tank hits $\geq$60 and veto hits $<$6 and that the time to a previous event with tank hits $\geq$100 or veto hits $\geq$6 was larger than 15 μs. This trigger was established to search for neutrinos from supernovae [10]. The tank hit requirement sets a lower energy threshold of $\sim$20 MeV, higher than optimal for a Supernova search, but necessary due to the high rate ($\sim$ 10 kHz) of β-decays in a near-surface detector. A supernova within 10 Kpc of the Earth is expected to produce a burst of these triggers at a rate at least 5 times greater than background. The rate of this trigger is $\sim$ 10 Hz.
- **Beam Gamma**: Requires tank hits $\geq$10, tank hits $<$100, and veto hits$<$4, within 1 ms of a beam event that contains a neutrino candidate, and no prior tank or veto activity within 15 μs. This trigger was designed to obtain a sample of $^1H(n,\gamma)D$ events (neutron capture) with the photon at 2.2 MeV, where the capture lifetime is 186 μs.
- **Beam Beta**: Requires tank hits $\geq$24 and veto hits $<$4 within 30 ms of a beam event that contains a neutrino candidate, and no prior tank or veto activity within 15 μs. This trigger is designed to select events from excited nuclei with longer lifetimes that will typically beta-decay within tens of ms after the neutrino event.
- **Strobe Gamma**: Same conditions as the Beam Gamma trigger, but is initiated by a Strobe trigger. Used to measure accidental rates.
- **Strobe Beta**: Same conditions as the Beam Beta trigger, but is initiated by a Strobe trigger. Used to measure accidental rates.
- **Tank**: Requires tank hits $\geq$60 and is prescaled. Used for detector monitoring.
- **Veto**: Requires veto hits $\geq$6 and is prescaled. Used for detector monitoring.
- **Laser**: Requires a calibration laser signal (Sec. 7.1). Used for detector calibration.
- **Fake Beam**: Requires a calibration beam signal. The laser is pulsed when the Booster extracts beam to the Main Injector instead of the MiniBooNE beam target. This provides a check on the effect that the accelerator operations may have on behavior of the PMT's and electronics.
- **Cube**: Requires a calibration cube signal which is set when the calibration cubes have detected a cosmic ray muon candidate. (see Sec. 7.2).
- **Tracker**: Requires a calibration tracker signal which is set when the cosmic-ray muon tracker has hits in all four tracking planes (see Sec. 7.2).

Every VME crate in the data acquisition (DAQ) system, including the trigger, contains a Motorola MVME 2604 single board computer, referred to as a "monoboard". This serves as the VME master as well as the resident 300 MHz PowerPC CPU to read data from the VME bus, send VME commands, run programs, and connect to the local DAQ network to send event data via 100 Mbit Ethernet. The boards are not equipped with hard drives, and must instead mount to the disks on the central DAQ computer. Each monoboard has a Linux kernel with only essential services and 64 Mbytes of memory. Each also has a serial port for the console and an Ethernet port used for data transfer and communications. Three rack-mounted computers are used for central data acquisition, processing, and monitoring. They also run the scripts associated with permanent data archival to Fermilab's Feynman Computing Center. All fourteen of the monoboards and the DAQ computers are connected via a 100 Mbit Ethernet hub to the internal MiniBooNE DAQ network.

The major components of the DAQ software are the QT software, trigger software (discussed in the previous section), the event-builder, run control, diagnostics, and archiving.

The QT software is a suite of C programs which run on the monoboards. The software uses address references to access the different VME functions. At the lowest level, a kernel driver checks the status of the TSA receiver and QT FIFO's 60 times/second. If the "empty flag" on the FIFO is not set, then the driver unloads data from the FIFO (via a VME interface). The advantage of using a driver instead of a conventional program is that it interrupts the running of any other code to unload FIFO's which fill rapidly making this a high-priority task. The driver makes the data available to the higher-level software for further processing. Next, each of the charge, time-ramp, and associated TSA data words are checked for inconsistencies. If any are found, error flags are set. Otherwise the data is compressed into good PMT hits, packaged with a header (TSA address) and sent via Ethernet to the central DAQ computer. The header contains the information needed to match the hits from all of the QT monoboards sending data.

The data required to reconstruct the charge and time for a PMT hit consist of the set of four consecutive digitized q and t ADC values starting with the 100 ns clock tick immediately preceding the hit. These eight values form a data "quad". Most PMT hits come in the form of quads, but occasionally, for high-energy hits, the charge ADC will saturate and, depending on the amplitude, will take as much as a few microseconds to stabilize. This condition is detected in the packaging software and causes it to extend the hit data up to 400 ns after the ADC values become unsaturated. PMT hits are detected in the online software through the presence of a ramp in the t ADC values. Data quads without a time ramp are ignored. This reduces the data stream by a factor of 100.

The first step in the procedure to convert a quad into PMT hit charges and times uses the first three t ADC values of the quad to determine t_{raw}, the raw time (in ns) that the discriminator fired relative to the clock tick that preceded it. Since a hit in the detector produces a known integrated charge shape, $V_q(t)$, in the electronics, the newly determined raw time can be used to predict the expected q ADC values for a given charge deposition. Hence, the raw charge, q_{raw}, is determined by finding the normalization of $V_q(t)$ that best fits the q ADC values associated with that hit. A charge-dependent time slewing correction, $t_{slew}(q)$, is taken from a lookup table indexed by q_{raw}; separate tables are used for the old PMT's and the new PMT's. The charge for saturated hits is determined by measuring the relaxation time of the integrator, since the charge amplitude is correlated with the integration relaxation time. This procedure is applied during offline data processing.

The event-builder collects Ethernet data packets from the QT monoboards and the trigger. When it receives a hit or set of hits from a crate, a status array indicates the existence of data from a crate. The data come asynchronously from the QT monoboards, and event-builder continues to listen for more data until all monoboards have sent charge and time data with matching TSA information. The trigger software also sends a packet of data showing all current trigger information that the event-builder merges with the data stream. It also performs integrity checks on the time information, and in particular, compares the trigger packet with the QT data packet. If a problem is found, then a new run is started, including an automated reset of all running software and VME devices. If not, the event is stored in binary format to disk. For every 100 Mbytes of data, a new file is created and numbered to allow easier manipulation and file transfer. At normal data taking rates, this occurs every 15 minutes, yielding a total data rate of ~100 kBytes/sec.

Once a new data-file is available, analysis scripts run on the file to monitor the health of the detector and subsystems. Thousands of plots such as PMT dark rates, tank and veto hit sums, *etc.*, are made available to the shift personnel to check the health of any aspect of the detector. Concurrently, the files are streamed from their original binary format to ROOT files which are written to tape along with the original files. The robotic tape system located at the Fermilab Feynman Computing Center facility is used for all tape archives. MiniBooNE has recorded approximately 18 Tbytes of raw data in five years of data taking.

Beam line, horn, and environmental data are merged offline with the detector data. All of the data streams are coordinated by the run control software which propagates time stamps and new run information to the other data stream's acquisition software in order to maintain uniform run boundaries. The most important of these external data streams is the beam line data which are acquired every beam spill using seven Internet Rack Monitors (IRM) and a "multiwire" front end. Each IRM collects data for one system: beam positions along the beam-line, beam loss monitors, beam position at target, target cooling system, horn system, beam intensity, and magnet power supplies. The "multiwire" front end records beam targeting information. Both the IRM's and multiwire front end push the data to the beam line data acquisition system, which bundles the data into a format allowing simple integration with the detector data. The state of the beam-line and proton beam can be reconstructed for each event. In particular, the number of protons incident on the target is recorded for each spill which allows for a more precise understanding of the neutrino flux.

7 Calibration Systems

7.1 Laser Calibration System

The MiniBooNE laser calibration system consists of a pulsed diode laser (PicoQuant GmBH PDL-800-B driver and LDH 375 laser head), and four dispersion flasks installed at various locations in the detector. Short pulses (<1 ns) of laser light with wavelengths peaked at 397 nm, are transmitted via optical fibers to each of the dispersion flasks. The primary purpose is to quantify and monitor individual PMT performance parameters. It also allows for *in-situ* monitoring of the oil attenuation length over the lifetime of the experiment. A schematic diagram of the laser/flask system is shown in Fig. 17. A switch box allows transmission of the laser light pulses to one of the dispersion flasks via an optical fiber. Each dispersion flask is 10 cm in diameter, filled with Ludox colloidal silica [11]; laser light sent to a flask illuminates all of the PMT's with approximately equal intensities. In addition to the four flasks, there is a bare optical fiber that emits light in a cone of $\sim 10^\circ$ opening angle, illuminating PMT's in a small circle near the bottom of the detector. It is used to study light scattering in the detector. The locations of the four flasks and the bare fiber are shown in Table 5; the coordinate system's origin is at the center of the detector, the z-axis points in the direction of the neutrino beam and the y-axis points in the vertical direction.

During normal data-taking, laser light is sent to the central dispersion flask (flask 1) at rate of 3.33 Hz, continuously and asynchronously with the accelerator. The laser system is vetoed by a beam extraction timing pulse and is thereby prevented from firing light into the detector during a beam event. The

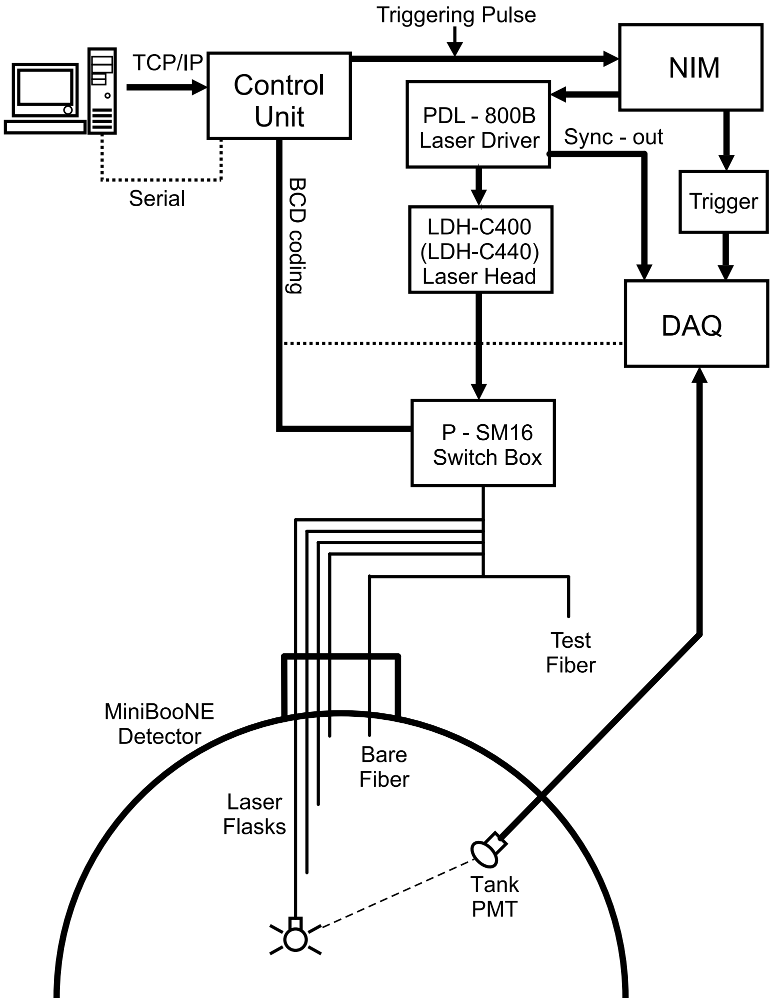

Fig. 17. Schematic diagram of the MiniBooNE laser calibration system.

Device	x (cm)	y (cm)	z (cm)
Flask 1	-0.3	-4.1	1.5
Flask 2	144.9	96.1	-126.4
Flask 3	1.7	-0.8	83.7
Flask 4	-80.0	203.9	-24.1
Bare fiber	82.0	540.0	65.0

Table 5
Positions of laser light sources in the MiniBooNE detector.

laser intensity is set to produce a low PMT occupancy; on average ~3% or 40 PMT's record hits in each laser event.

The raw PMT hit times described in Sec. 6.4 are transformed into calibrated times using individual time offset constants, one for each PMT. The raw PMT charges are normalized into units of photoelectrons by individual multiplicative gain calibration constants, one for each PMT. These calibration constants are extracted from the laser calibration data. The time offset is used to account for transit time differences in each PMT/QT readout channel. These time offsets are calculated by measuring the difference between the observed time of each PMT hit and the known time of the laser pulse, with corrections for the laser light time-of-flight. The gain calibration constant is used to account for individual differences in the gains of PMT's. The gain constants are calculated by defining the mean of the q_{raw} distributions from calibration laser events to have the value of one photoelectron. A correction for Poisson fluctuations in the actual number of photoelectrons observed is made, using the measured average occupancy for calibration laser events. To account for charge dependent time-slewing, a time slewing lookup table is created using calibration laser events. The table is indexed by the raw (not gain calibrated) charge, q_{raw}, because it depends on the amount of charge seen by the ADC's, not on the number of photoelectrons hitting the PMT.

Single photoelectron charge distributions are also extracted from the laser calibration data (one for each type of PMT), and are used as inputs to the Mont Carlo simulation of the detector.

7.2 Cosmic Muon Calibration System

The muon calibration system hardware consists of a scintillator hodoscope located above the detector and seven scintillator cubes deployed within the detector signal region. A distinct signature is produced when a muon passes through the muon tracker, stops in a scintillation cube, and decays. The muon produces Cherenkov light that is detected by the tank PMT's as well as a coincident signal in the scintillator cube. When it decays, the resulting Michel electron also produces coincident signals as it exits the cube and traverses the tank volume. Such events, where the location and momentum of the muon and the origin of the electron can be independently determined from the muon hodoscope and cube geometry, provide a means of tuning and verifying event reconstruction algorithms.

The hodoscope has two layers of plastic scintillator, each with an x and y plane, that determine the positions and directions of muons entering the detector. The scintillator strip widths in the muon tracker and the separation between the planes were chosen to give adequate coverage throughout the entire detector and to have a reconstruction angular resolution that would be dominated by the effects of multiple scattering of the muon as it passes through the detector; the RMS resolution of the muon tracker itself is $\sim 1.9^\circ$ (34 mrad).

Cube depth (cm)	x (cm)	y (cm)	z (cm)	$< Range >$ (g/cm^2)	$< T_\mu >$ (MeV)
31.3	-60.8	540.7	15.1	28. ± 1.	95. ± 4.
60.3	15.6	511.7	-57.6	54. ± 2.	155. ± 5.
100.5	57.9	471.5	-13.5	89. ± 3.	229. ± 7.
200.8	-18.6	371.2	59.2	174. ± 4.	407. ± 9.
298.1	40.8	273.9	44.5	256. ± 4.	584. ± 9.
401.9	40.8	170.1	44.5	344. ± 4.	771. ± 9.

Table 6
Positions of cosmic muon calibration cubes. The depth is the distance of the center of the cube below the optical barrier. $< Range >$ is the average material, within the detector signal region, traversed by muons that pass through the muon tracker and stop in the cube. $< T_\mu >$ is the kinetic energy of the muon as it enters the signal region. The range uncertainty shown is the RMS of the range reconstructed for data events from the geometry of the hodoscope and cubes. It is propagated into the kinetic energy uncertainty using the range-energy table from Ref. [13], with an additional contribution from straggling.

The positions of the cubes in the detector vary from 15 cm to 400 cm from the optical barrier, so that stopping muons from 20 MeV to 800 MeV can be measured. Each 5-cm cube is housed in a sealed aluminum box and has an optical fiber leading to a 1 inch PMT for readout. The deepest cube is larger, 7.6 cm on each side, to increase its signal rate. One cube is deployed with a special optical barrier that blocks light produced behind the PMT's, reducing the total path length for muons stopping in it to ~11 cm; that cube is not used in the results discussed here. The positions of the cubes in the tank were surveyed by the Fermilab alignment group; the reported error on their measurements is less than 3 cm [12]; the depths of the shallow cubes were measured by hand during the installation. The cube positions are given in Table 6.

The time and charge measurements of each cube are calibrated with through-going muons. The charge gain calibration for each cube is performed by finding the mean in the charge distributions of through-going muon events, assuming that each muon is minimum ionizing. The time calibration results in a time offset such that the cube PMT hit matches the muon event time as measured by the main detector. The rate of muons passing through the muon tracker and one cube is approximately half a Hertz, and the rate of muons stopping in the cubes is approximately 100 per month.

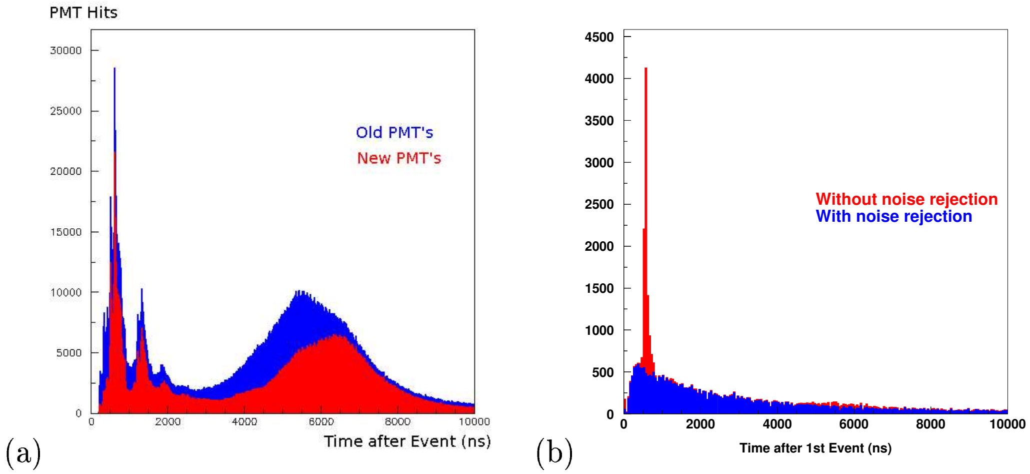

Fig. 18. (a) Time distribution of PMT hits occurring after an energetic cosmic ray event. Triggers that contained multiple hit clusters with high charge have been excluded from this plot in order to remove muon decays and triggers with more than one cosmic ray. (b) Time distribution of event clusters following an energetic cosmic ray event with and without the noise rejection filter. The filter removes the peaks due to coherent PMT noise without distorting the underlying distribution expected from muon decays.

8 Detector Performance

8.1 Event Definition

As described in Sec. 6.3, a beam trigger records all PMT signals that occurred in a 19.2 μs time window beginning approximately 5 μs before the arrival of the neutrino beam regardless of whether or not there were any interactions. Therefore the first step in any analysis is to isolate those signals caused by interactions in the detector. This is done by looking for clusters of PMT hits in time. A neutrino interaction can generate multiple time clusters depending on the type of interaction. A ν_μ charged current quasi-elastic (CCQE) interaction will typically generate two clusters; one from the muon produced in the initial reaction, followed by a delayed cluster from the Michel electron produced by the muon decay at rest. CCQE interactions of ν_e's will produce only single clusters. An event is defined as a trigger containing at least one cluster and we refer to the individual clusters that make up an event as subevents.

Clearly the number of subevents present in an event is an important clue to determining what type of event it is. The algorithm used to find subevents must therefore be both efficient and background-free. The one used in this experiment starts off by defining a seed cluster as a group of at least 10 hits for which the largest time difference between any two consecutive hits is less than 10 ns. Once a seed cluster is found it is extended to include late hits provided there are no time gaps of more the 20 ns and no more than two time gaps greater than 10 ns. This extension was required to pick up late PMT hits from scintillation light that might otherwise have been wrongly indentified as a second subevent. Monte Carlo studies found no cases where this algorithm left out more than 10 PMT hits that should have been assigned to a subevent.

Events that generate a lot of light in the detector were found to also generate a small amount of coherent noise in the PMT's that could produce fake subevents. The noise hits have low charge and exhibit a distinctive time structure as shown in Fig. 18 (a). The clustering algorithm uses this time structure to calculate the likelihood that any given PMT hit was due to noise. This is then used to reject these fake subevents. Figure 18 (b) shows the effect of applying the noise rejection to hit clusters that occurred after an energetic cosmic ray event.

Using Monte Carlo generated Michel decays and ν_e CCQE interactions, it was determined that the algorithm's efficiency at finding electron subevents increases from 99.5% for 10 MeV/c momentum electrons to 100% for momenta above 100 MeV/c.

8.2 Muon Energy and Angle Resolution

The muon energy and angular resolution of the detector are measured using the cosmic muon calibration system described in Sec. 7.2. The selection of cosmic muon events requires a clean reconstruction using the muon tracker and exactly two subevents in the tank with appropriate cuts on the number of PMT hits in each subevent.

We measure the range in oil using muons that pass through the muon tracker and stop in the scintillation cubes; the measured range is used to calculate the muon kinetic energy. The stopping muon events are selected by matching the times of tank subevents with cube hits, and appropriate cuts on the charge of the cube hit. The event sample is refined further by requiring the reconstructed Michel electron position be near the cube position.

The two points obtained from the muon tracker and the position of the cube are used in a fit to a straight line whose intersection with the optical barrier of the detector gives the muon's entry point. The distance from this entry point to the cube's position gives the muon's range. From this, the energy is determined using a lookup table [13] for muon range in polyethylene with the measured density of the MiniBooNE oil.

The energy resolution is calculated from the fractional difference of kinetic energies obtained from the detector event fitter [14], T_μ^{DET}, and the cube

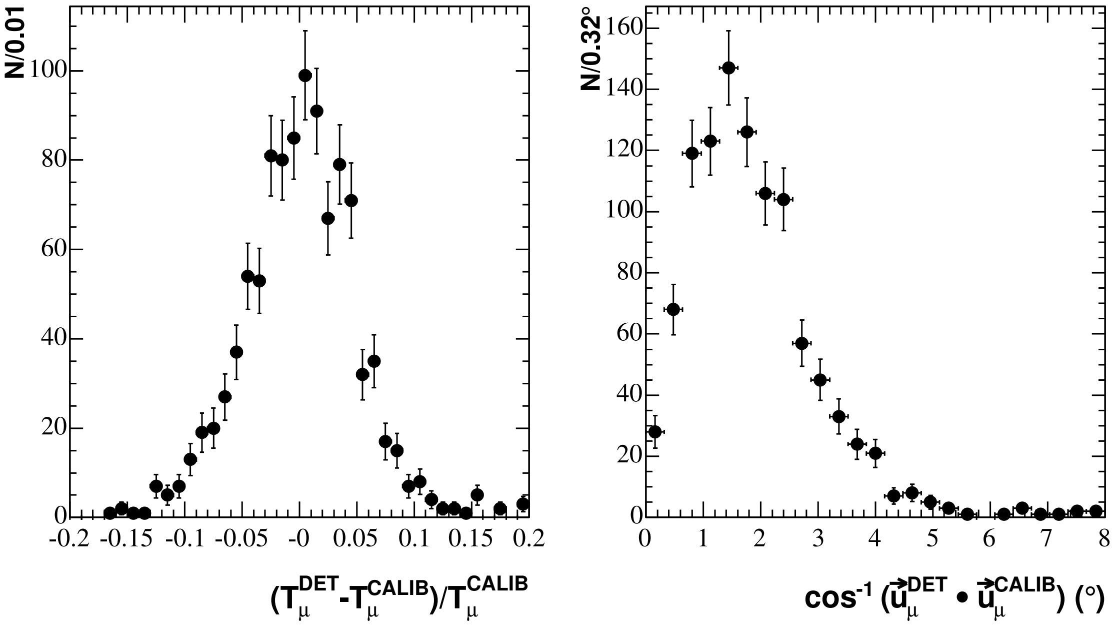

Fig. 19. Energy and angle resolution for reconstruction of cosmic muons found using the 2 m deep cube ($< T >$=407 MeV).

$< T >$ (MeV)	Angular Resolution	Energy Resolution
95. ± 4.	5.4°	12%
155. ± 5.	3.2°	7.0%
229. ± 7.	2.2°	7.5%
407. ± 9.	1.4°	4.6%
584. ± 9.	1.1°	4.2%
771. ± 9.	1.0°	3.4%

Table 7
The muon angle and kinetic energy resolution for each cube. The first column is repeated from Table 6

track length calculation, T_μ^{CALIB}. Figure 19 shows the differences calculated for cosmic muons stopping in the 2-m-deep cube. The distribution is fitted to a Gaussian function whose width gives the energy resolution. The kinetic energy resolution for each cube is shown in Table 7; the energy resolution thus extracted includes comparable contributions from T_μ^{DET} and T_μ^{CALIB} and is dominated by range straggling [15] and the sizes of the cubes themselves.

To study the angular resolution, we compare the direction vectors from the detector event fitter, $\vec{u}_\mu^{DET}$ and the muon tracker, $\vec{u}_\mu^{CALIB}$. The distribution of the angular difference between these vectors for muon events stopping in the 2 m deep cube is shown in Fig. 19. We fit the distribution to the function

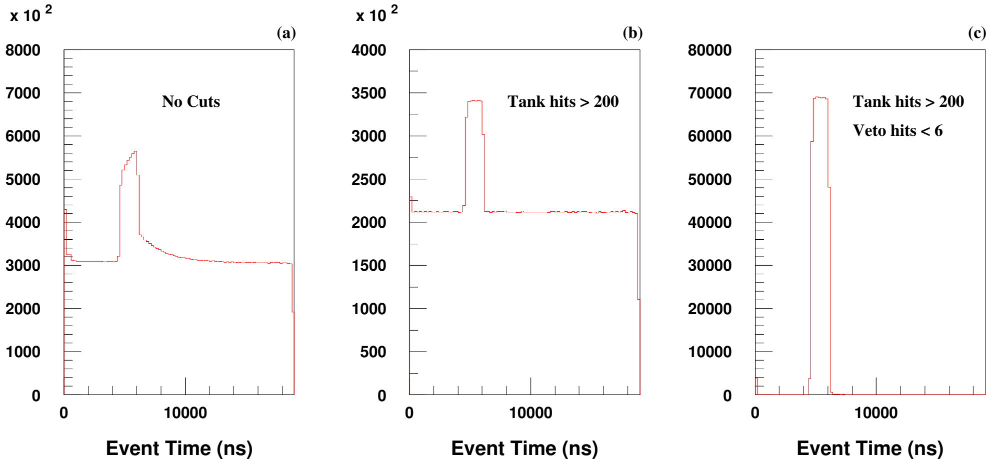

Fig. 20. Time distributions of subevents within the 19.8 μ-sec beam window: a) with no cuts, b) subevents with more than 200 tank PMT hits, and c) subevents with more than 200 tank PMT hits and fewer than 6 veto PMT hits.

$N(\theta) = c \cdot \theta\, \mathrm{e}^{-\theta^2/2\sigma_\mu^2}$, under the assumption that the distribution represents the projection of a symmetric two dimensional Gaussian distribution onto the radial axis. The width of the Gaussian function, σ_μ, gives the muon angular resolution. The results for each cube are summarized in Table 7.

8.3 Isolating Neutrino Interactions

Figure 20 shows time distributions of subevents within the beam trigger windows. Figure 20 (a) contains all subevents without cuts and clearly exhibits the three main components: a flat cosmic ray background, neutrino beam interactions which have a flat distribution starting at about 4.5 μs and lasting for 1.6 μs, and Michel electrons from the decays of muons produced in the neutrino interactions. The latter exhibit an exponential fall off after the end of the beam spill and rise as 1 minus an exponential during the spill. The exponential constants are characterized by the muon lifetime. The pile up of events at the beginning of the trigger window is due to cosmic rays that occurred just before the trigger and were still depositing light in the tank when the readout started.

The first step in isolating subevents due to neutrino interactions is to remove the low-energy ones produced by Michel electrons. This is done by rejecting subevents with fewer than 200 PMT hits in the signal region of the main tank and the result is shown in Fig. 20 (b). The remaining cosmic ray background is removed by applying a cut on the number of PMT hits in the veto region

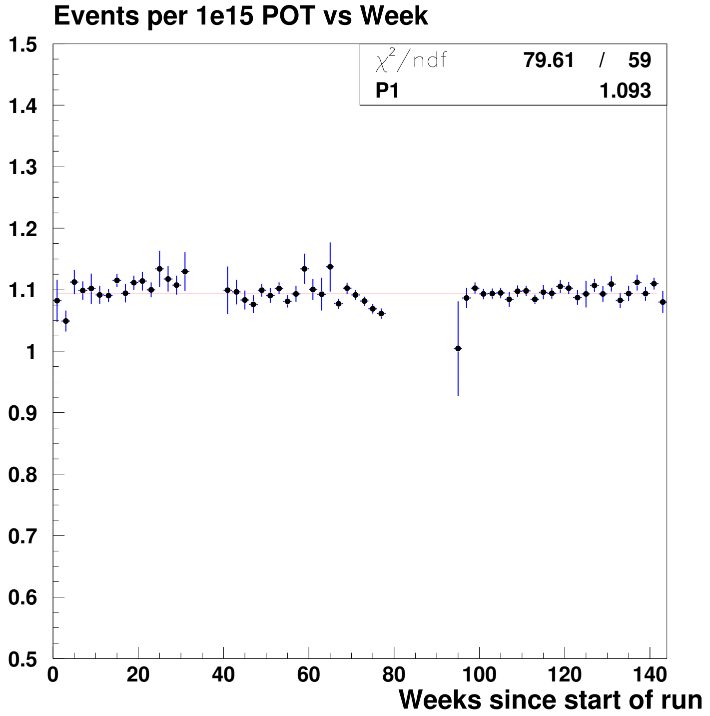

Fig. 21. Neutrino interactions per beam proton as a function of time.

of the detector. Keeping only subevents with fewer than 6 veto hits reduces the cosmic ray background by a factor of 10^4 and leaves a very clean sample of beam neutrino interactions as shown in Fig. 20 (c). Applying these cuts to a high statistics sample of Strobe triggers, we obtain a veto efficiency of 99.987% for cosmic ray events above the Michel electron energy cutoff.

With a cleanly isolated sample of beam neutrino interactions, one can check the stability of the detector and beam by monitoring the number of neutrino interactions detected per proton on target (POT). In Fig. 21 this ratio is plotted as a function of time over the 3 years in which MinBooNE collected neutrino data. Statistical errors only are used in the flat line fit to this data and the resulting χ^2 per degree of freedom is consistent with a less than 1% week-to-week systematic error on the measurement of the protons on target. There is no evidence of a long term trend that one might expect if, for instance, the detector oil purity had been deteriorating. Instead, the data indicate that the detector has performed well and remained stable since 2002 when it was first commissioned.

9 Acknowledgments

The authors acknowledge the support of Fermilab, the Department of Energy, and the National Science Foundation. We thank Los Alamos National Laboratory (LANL) for LDRD funding. We also acknowledge Dmitri Toptygin and Anna Pla for optical measurements of the mineral oil. The MiniBooNE detector could not have been built without the support provided by Fermilab, Los Alamos, and Princeton University technicians. In particular Andy Lathrop from the Fermilab Mechanical Department was crucial to the installation and maintenance of the various utilities, including the nitrogen gas system. Camilo Espinoza and Neil Thompson from LANL played a major role in the installation of the oil plumbing and detector electronics. Ben Sapp, Shawn McKenney, and Nate Walbridge from LANL were instrumental in the development and installation of the DAQ hardware and software. The PMT testing and preparation owed much to the efforts of Fermilab technicians, Sabina Aponte, Lyudmila Mokhov, and Galina Terechkina. Hayes Lansford provided invaluable assistance with the tank scaffolding and installation and finally, we would like to thank Princeton technicians, William Groom, Stan Chidzik, and Robert Klemmer for their work on the fabrication and installation of the PMT support structure.

References

[1] A. Aguilar *et al.*, Phys. Rev. **D64**, 112007 (2001).

[2] A. A. Aguilar-Arevalo *et al.*, "The Neutrino Flux Prediction at MiniBoooNE" (paper submitted for publication: arXiv:0806.1449).

[3] B.T. Fleming, L. Bugel, E. Hawker, V. Sandberg, S. Koutsoliotas, S. McKenney and D. Smith, IEEE Trans. Nucl. Sci. **49**, 984 (2002).

[4] PMT efficiency data is from Hamamatsu Corp., D. Lowell, private communication, July 6, 2004. It includes transmission through the glass, and this has been corrected in the figure for the smaller reflection that occurs when the PMT is in oil.

[5] S. J. Brice *et al.*, Nucl. Instrum. Methods, **A562**, 97 (2006).

[6] J. L. Raaf *et al.*, IEEE Trans. Nucl. Sci. **49**, 957 (2002).

[7] B. C. Brown *et al.*, IEEE Nuclear Science Symposium Conference Record 1, 652 (2004).

[8] C. Athanassopoulos *et al.*, Nucl. Instrum. Methods, **A388**, 149 (1997).

[9] E. Ables *et al.*, FERMILAB-PROPOSAL-0875.

[10] M. K. Sharp, J. F. Beacom, J. A. Formaggio, Phys.Rev. D66 (2002) 013012

[11] Ludox is a registered trademark of W. R. Grace Davison.

[12] B. O. Oshinowo, Proceedings of 7th International Workshop on Accelerator Alignment (IWAA 2002), SPring-8, Japan, 11-14 Nov 2002, pp 021 (FERMILAB-CONF-02-425).

[13] `http://pdg.lbl.gov/AtomicNuclearProperties`.

[14] R. B. Patterson *et al.*, "The Extended-Track Event Reconstruction for MiniBooNE" (paper in preparation).

[15] R. M. Sternheimer, Phys. Rev. **117**, 485 (1960).